UNIVERSITY OF CALIFORNIA
RIVERSIDE

# Development and Characterizations of 2D Thin Films and Quasi 1D Nanowires Towards Practical Downscaled Integrated Circuits

A Dissertation submitted in partial satisfaction
of the requirements for the degree of

Doctor of Philosophy

in

Chemistry

by

Thomas A. Empante

September 2019

Dissertation Committee:
Dr. Ludwig Bartels, Chairperson
Dr. De-en Jiang
Dr. Boniface Fokwa

The Dissertation of Thomas A. Empante is approved:

_____

_____

_____

Committee Chairperson

University of California Riverside

ABSTRACT OF THE DISSERTATION

Development and Characterizations of 2D Thin Films and Quasi 1D Nanowires
Towards Practical Downscaled Integrated Circuits

by

Thomas A. Empante

Doctor of Philosophy, Graduate Program in Chemistry
University of California, Riverside, September 2019
Dr. Ludwig Bartels, Chairperson

Electronic devices utilize the foremost advances in technology. In order to make progress we must understand not only the properties of novel materials but also how best to synthesize these materials in an appropriate way so that they can be used in an industrial setting.

Transition metal dichalcogenides, specifically molybdenum ditelluride ($MoTe_2$) is a class of 2D material that has been well studied for their semiconducting nature in the 2H phase yet they also have 2 other phases with vastly different properties: 1T' and 1T. The 1T' phase has metallic properties. There is a 3$^{rd}$ phase, however, that prior to my work has been largely left unstudied, the 1T phase. This phase is calculated to be semi metallic from its calculated band structure but is also highly unfavorable at room temperature. With this in mind we set out to synthesis this elusive phase via a chemical vapor deposition process by selectively using process gases and varying cooling rates to stabilize the 1T phase at ambient temperatures. Measurements confirm the 1T phase of $MoTe_2$ is in fact semi-metallic. In addition, mixed phase 2H/1T films were synthesized and electronically tested

to yield a semiconducting film with significantly improved conductivity that could still be gated for on/off current switching.

As copper interconnects decrease in cross-section to below 100 nm in size the resistivity of this, typically, highly conductive metal starts to increase exponentially do to surface and grain boundary scattering of electrons. Quasi-1D Transition metal trichalcogenides, like tantalum triselenide ($TaSe_3$), can have metallic properties. The main issue that is being addressed is that of copper interconnects as they reach their scaling limits. The concentration is 2-fold, 1) develop a growth method/process that could synthesis $TaSe_3$ at temperatures at or lower than 400°C and 2) measure the materials resistivity as a function of decreasing cross-sectional area to see if these highly crystalline transition metal trichalcogenide maintains its bulk resistivity unlike that of copper. Given this momentous task we again set out to develop a chemical vapor deposition process to synthesis $TaSe_3$ using volatilized reagents to help aid in the formation of the crystals at low temperatures. The resistivity of the nanowires grown using this method were tested down to 7nm in cross-sectional area and found no scaling effect present with regards to resistivity. In addition, it was also found to have an electromigration activation energy, the main failing point of interconnects, to be double that of copper and able to withstand current densities of $10^8$ A/cm$^2$, orders of magnitude higher than copper. The results give credence to this class of materials potential for future downscaled devices.

# Table of Contents

# List of Publications

**Empante, T. A.**; Martinez, A.; Wurch, M.; Zhu, Y. B.; Geremew, A. K.; Yamaguchi, K.; Isarraraz, M.; Rumyantsev, S.; Reed, E. J.; Balandin, A. A.; Bartels, L., Low Resistivity and High Breakdown Current Density of 10 nm Diameter van der Waals $TaSe_3$ Nanowires by Chemical Vapor Deposition. Nano Letters **2019**, 19 (7), 4355-4361.

Maiti, R.; Hemnani, R. A.; Amin, R.; Ma, Z. Z.; Tahersima, M. H.; **Empante, T. A.**; Dalir, H.; Agarwal, R.; Bartels, L.; Sorger, V. J., A semi-empirical integrated microring cavity approach for 2D material optical index identification at 1.55 μm. Nanophotonics **2019**, 8 (3), 435-441.

Almeida, K.; Wurch, M.; Geremew, A.; Yamaguchi, K.; **Empante, T. A.**; Valentin, M. D.; Gomez, M.; Berges, A. J.; Stecklein, G.; Rumyantsev, S.; Martinez, J.; Balandin, A. A.; Bartels, L., High-Vacuum Particulate-Free Deposition of Wafer-Scale Mono-, Bi-, and Trilayer Molybdenum Disulfide with Superior Transport Properties. ACS Applied Materials & Interfaces **2018**, 10 (39), 33457-33463.

**Empante, T. A**.; Zhou, Y.; Klee, V.; Nguyen, A. E.; Lu, I. H.; Valentin, M. D.; Naghibi Alvillar, S. A.; Preciado, E.; Berges, A. J.; Merida, C. S.; Gomez, M.; Bobek, S.; Isarraraz, M.; Reed, E. J.; Bartels, L., Chemical Vapor Deposition Growth of Few-Layer $MoTe_2$ in the 2H, 1T′, and 1T Phases: Tunable Properties of $MoTe_2$ Films. ACS Nano **2017**, 11, 900-905.

Jia, H.; Yang, R.; Nguyen, A. E.; Alvillar, S. N.; **Empante, T.**; Bartels, L.; Feng, P. X. L., Large-scale arrays of single- and few-layer $MoS_2$ nanomechanical resonators. Nanoscale **2016**, 8 (20), 10677-10685.

## List of Figures

# Chapter 1: Motivation

## 1.1 Motivation

Most random-access memory (RAM) devices use volatile memory elements which are subject to data loss if the system loses power. One way to stop this from happening is to use non-volatile memory in the system. Non-volatile memory, like flash drives, work well in the short term as an intermediate fix but have a downside, the slow write times. Another type of non-volatile memory is phase change memory. This relies on the material being used to physically change the phase of the material between device channels, generally with quick burst of heat, in order to "write" information down and save. The change in materials phase will make the resistivity change, generally between one crystal phase and one amorphous phase, this process will allow the memory device to read the resistivities and create a non-volatile element of memory that doesn't forget its information if the chip loses power. In order to understand a materials viability as a phase change material each phase of a material must be known and well characterized. Toward this effort the TMD $MoTe_2$ has been studied and analyzed in 2 phases but there is third unaccounted phase that needs to be 1) synthesized and 2) characterized to see if the calculated properties are indeed a reality.

As devices decrease in size each year the scaling issues arise. One of the major issues that the industry is dealing with today is the failing efficiency of device interconnects. Interconnects the powerlines of a device's circuitry, supplying power to all of the elements on the chip. Today these interconnects are made of copper, which is one of the most

conductive metals on the periodic table having a bulk resistivity of 1.7μΩcm. However, as the interconnect downscales, its cross-section gets smaller which limits the amount of space the electrons can flow through. This leads to the electrons having a higher number of collisions with grains of the metal (grain boundary scattering) and with the walls of the interconnect (surface scattering). As the cross-section reaches coppers mean free path, ~40 nm, the resistivity starts to increase drastically and as it decreases even farther the below the mean free path starts to increase exponentially. This is a problem for two reasons, one, this leads to a decrease in the amount of current density the copper interconnect can handle and two, leads to high collision rates with the copper atoms themselves which can create voids in the interconnect and therefore broken connections, the leading cause of device failure. The mitigate these problems a new material will need to take coppers place as the interconnect material. One such class of material are transition metal trichalcogenides which are highly crystalline materials that can have metallic properties. The problem lies in the synthesis of the material in situ, as part of the device making process but has only previously been made with incompatible methods. Here we develop a novel method of synthesizing the TMT $TaSe_3$ with a more BEOL compatible process for potential implementation in future nanoscale devices.

# Chapter 2: History of Relevant Materials

## 2.1 Transition Metal Dichalcogenides

Transition metal dichalcogenides, particularly $MoS_2$, were first discovered in 1778 as naturally occurring molybdenite minerals by Swedish Chemist Carl Wilhelm Scheele.[1] It was mainly mined in the geographical region of Norway, namely the Knaben mine but was left unstudied until the start of World War I when new mines in Colorado opened up to supply the military with a source of molybdenum which was used as an additive to steel for better tank armor and later in early 1940's research in the application of molybdenite ($MoS_2$) as a dry lubricant.[2-6] It wasn't until the late 1950's when Richard Feynman[7, 8] speculated the future importance of layered materials that sparked researchers to put more focus back onto TMDs for further exploitation of its structurally layered nature. It was not long after this classic lecture that $MoS_2$'s optical properties were characterized with decreasing layers exfoliated from these naturally formed molybdenite crystals using "sticky tape" by Robert Frindt[9] probing the optical absorption and photoconductive nature of the bulk material. A number of chemical exfoliation methods were developed to study lower layered TMD materials, most notably, for metallic TMDs like $TaS_2$[10, 11] and $NbS_2$[11] and later for semiconducting $MoS_2$[12] in 1986 by Per Joensen (along with Frindt and Morrison). Later research in the 1970's showed that $MoS_2$ had catalytic properties that aided in hydrodesulfurization reactions[12-17] which are used by oil industry for the production of higher purity products till this day. With the advent of novel micromechanical exfoliation techniques, most notably by Novoselov[18] for graphene, the emergence of multiple reports in the early 2010's found that the mono layer of $MoS_2$

exhibits a photolumenesence at the energy of 1.84eV corresponding to the transition to a direct band gap at the monolayer from an indirect band gap in the bulk. [19-22] The discovery of the monolayered TMD material allowed for a vast amount of research to take place and discovered a plethora of exciting properties such as field effect transistors (FET), valleytronic behavior[23-25] and suggests the potential for spintronic applications[26] due to absence of inversion symmetry leading to spin orbit coupling in the Brillion zone near the K-point. The optical band gap for molybdenum based TMDs, $MoS_2$, $MoSe_2$, and $MoTe_2$ are 1.84eV, 1.55eV, and 1.1eV respectively. The band gap of $MoTe_2$ is relatively low and has been proposed for applications in silicon-based photonics. [19, 20, 27] While $MoS_2$ and $MoSe_2$ have been studied extensively, $MoTe_2$ has had comparatively little research performed on it. This is due to the materials proclivity for oxidation in air like that of bare silicon[28, 29]. In this thesis every synthesized $MoTe_2$ sample was spun coat with a layer of poly-methyl methacrylate (PMMA) in an inert environment, nitrogen filled glovebox (see figure 3.9), to mitigate the amount of oxidation to great success.

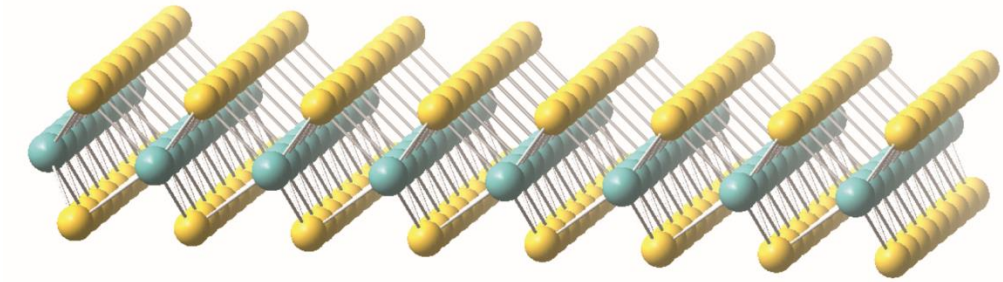

**Figure 2.1:** Ball and stick depiction of $MoS_2$ showing the molybdenum atom layer, greenish-blue, sandwiched between two sulfur layers, yellow, illustrating the single layer nature of TMDs.

### 2.1.1 Phases

As mentioned above some TMDs like $TaS_2$ and $NbS_2$ have metallic properties, whereas for molybdenum based TMDs have semiconducting properties. This is due to the fundamental crystal phase of the material which for $MoS_2$, $MoSe_2$ and $MoTe_2$ is the 2H trigonal prismatic semiconducting phase. However, this is not the only phase these materials can have. In addition to the 2H phase there is an octahedral structure known as the 1T phase and a 2x1 reconstruction of the 1T phase which is metallic known as the 1T' phase (see figure 2.2). [22, 30, 31] For $MoTe_2$, the as yet synthesized 1T phase is predicted to have a semi-metallic behavior.[32, 33]

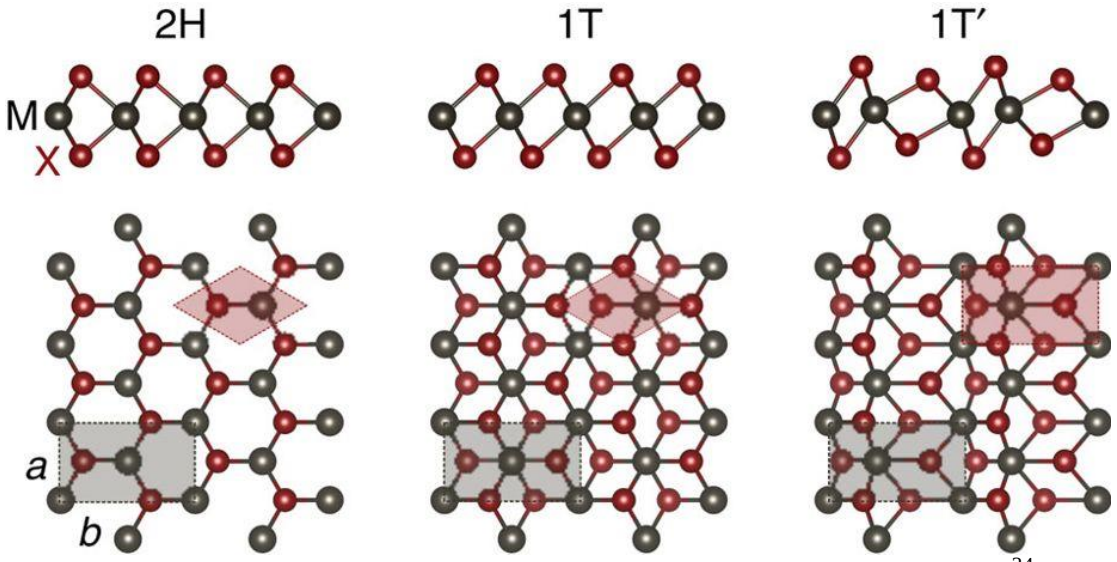


**Figure 2.2:** Top and side view of the 2H, 1T, and 1T' phases of $MoTe_2$[34]

Previous reports on the phase changing properties of $MoTe_2$ have been exclusively on the 2H and the 1T' phases.[34-37] with the vast majority coming from exfoliated bulk chemical vapor transport (CVT) crystals[38-43] with the exceptions of references[44-46]. While these CVT grown materials can synthesize high quality crystals the method lacks the

controllable means of phase selectivity and while chemical treatments can be used to change the phase of the material it inherently causes defects in the crystal lattice. Reports have calculated that the 1T' phase of the material can be favored during processing[47] if you use particular process gases during the synthesis process. Since the 1T' is the reconstructed version of the 1T phase it stands to reason that it could help favor the formation of the 1T phases as well. This phase is the prime objective of the research. The stability or pseudo stability of the 1T phase at ambient temperatures is the primary goal. For this reason, the CVD[45, 46] method described in section (3.4.1) was developed to allow the growth of not only the 2H and1T' phases but also the novel 1T phase.

### 2.1.2 Electronic Properties

The electrical properties of a material are dependent on the energies of the electrons in the conduction and valence bands. These bands have a distinct momentum of electrons as a function of position in the crystal lattice. When the electrons in the highest occupied molecular orbital (HOMO), valence band, overlap in energy with the lowest unoccupied molecular orbital (LUMO), conduction band, the material is metallic. Conversely if the HOMO and LUMO band energies have a gap between them on the order of <3.5 eV then the material is semiconducting and insulating if the gap is larger than 3.5 eV. If the materials HOMO and LUMO bands are at the same energy level but do not touch the material is said to be semi-metallic. It has been calculated that the 1T phase of $MoTe_2$'s band diagram indicates the phase is a semi-metallic material (see figure 4.4).

## 2.2 Transition Metal Trichalcogenides

Transition metal trichalcogenides, unlike there dichalcogenide sister compounds, are not geologically found in nature and were first synthesized in 1938 by Biltz describing the synthesis of $TaS_3$ via a CVT like process.[48] In the years that followed other TMTs were grown, like that of $TaSe_3$[49-51], and characterized to further elucidate the rod like structural nature of these TMT materials. In the late 1970s focus was again put on the TMTs when the conductivity of these materials were being measured for charge density wave (CDW) properties.[52, 53] Noticeably all of the synthesis methods for attaining TMTs are via CVT, which is mentioned in section 3.4, and can produces high quality crystals. However, the CVT process has massive drawbacks when it comes to synthesizing materials. Firstly, it requires the reaction to be performed in a sealed quartz tube that is evacuated and filled with a process gas, usually a halogen like iodine or bromine. Second, the process uses synthesis temperatures of over 900°C for periods of 72 hours to over 1 week which are excessively long for high throughput processes. Third, the resulting crystals that the process yields are bulk crystals which, for any nanoscale characterization need to be exfoliated and transferred to a substrate in order to be characterized. This method is largely unfit for any type of industrial application. The ideal process for any industrial purpose needs synthesis temperatures below 400°C for brief periods of time.

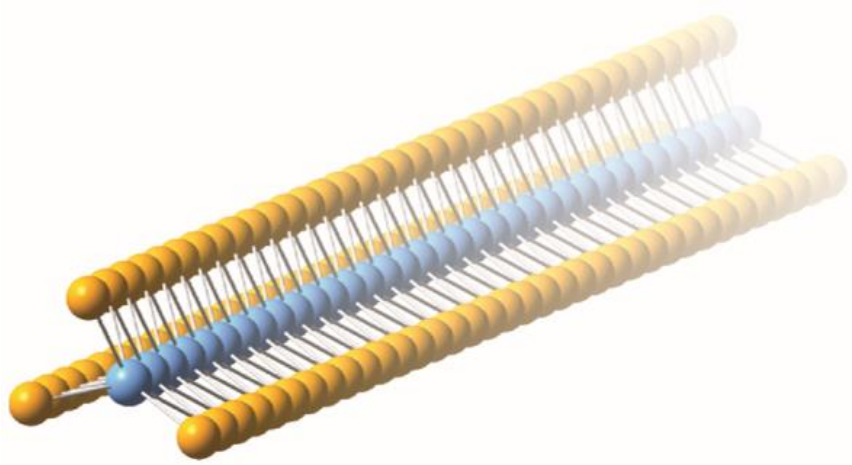

**Figure 2.3:** Ball and stick illustration to show the rod like nature of transition metal trichalcogenide nanorods

The applications for low dimensional materials like TMDs[21, 54-58], graphene[18, 59-61], and MXenes[62-65] has pushed the boundaries of technology as we know it. One thing that most of these materials have in common is a van der Waals gap in their crystal structure that aid in there layer like nature, optoelectronic properties, and reduced scattering in transport. TMTs also have a van der Waal gap like that of TMDs but instead of being planar they are tubular and surround the rod like structure of the trichalcogenide. Recently published transport measurements on metallic 1D $TaSe_3$ [66-68] and zirconium tritelluride ($ZrTe_3$)[69] showed bulk conductivity and high breakdown current density threshold on mesoscopic exfoliated bundles, respectively. In the CVD section (see 3.4) we describe our novel chemical vapor deposition (CVD) process that allows the fabrication of wire bundles as small as a few nanometers across (i.e. consisting of a hundred atom stacks or less in parallel), scaled to the demand of the semiconductor industry for upcoming processing nodes.

### 3.2 Electronic Properties

As electronic devices continue to downscale in size new problems arise with regards to the number of devices per area can be fabricated on a chip. One of the major issues that is starting to take precedence is the exponentially increasing resistivity of copper

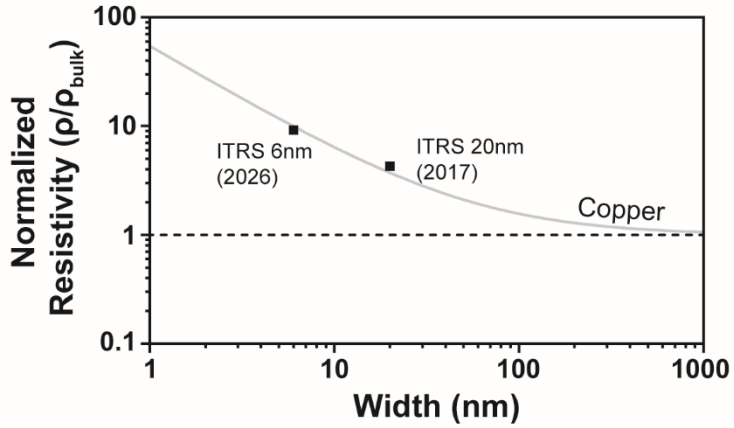


**Figure 2.4:** The change in the normalized resistivity of copper interconnects as the cross-section is scaled down to 1 nm.

interconnects as you scale down its cross-section. In an effort to understand the behavior of TMTs as the materials cross-section is scaled down. we find that such nanoscale bundles retain the bulk conductivity, much different to conventional metals, which at the 10 nm cross section scale are strongly affected by surface and grain-boundary scattering.[70-72] Additionally, we find that $TaSe_3$ exhibits a barrier to electromigration more than twice that of copper and can sustain current densities in excess of $10^8$ A/cm$^2$. The favorable scaling of the conductivity with wire cross section renders these material of great interest as next generation interconnect material as copper reaches its scaling limits in 2023 according to the ITRS roadmap.[73-76]

# Chapter 3: Experimental Techniques

### 3.1 Raman Spectroscopy

Raman spectroscopy is a useful characterization technique for determining the lattice vibrations of the crystalline material that is discussed in this thesis. This, non-destructive, technique relies on measuring the way a material scatters photons inelastically, namely by that of Stokes and, to a lesser degree, anti-stokes interaction. When you expose a crystalline material to a specific wavelength (energy) via a laser the electrons in the material are excited to a higher energy state.

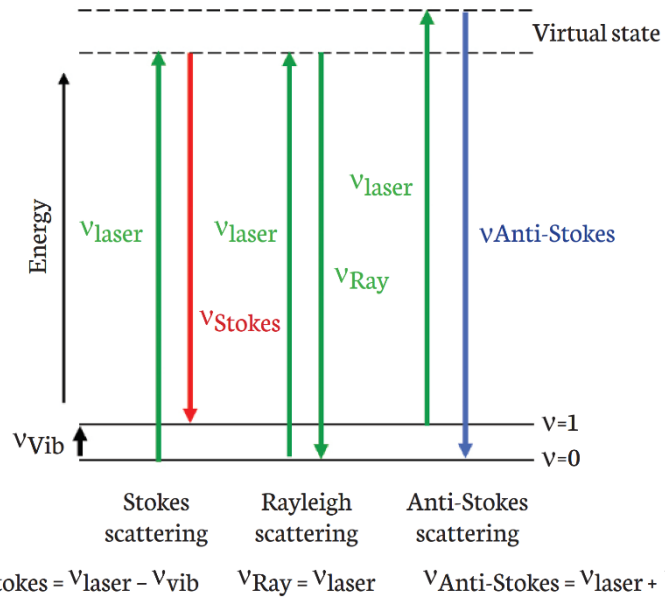


**Figure 3.1:** Depiction of the excitation of electrons in a molecule to an excited virtual state and relaxing to give Stokes and Anti-Stokes lines measured in Raman spectroscopy.[77]

The difference in energy measured from the incident light and the 1st excited vibrational state gives the vibrational energy of the bonded atoms in the crystal lattice. The spectra attained is a fingerprint of the chemical bonds in the system and helps identify and confirm the material synthesized in the growth process is the accurate material. Other characterization techniques like that of FTIR rely on inducing a dipole in the molecule rather than polarizability in Raman spectroscopy. We use a Horiba LabRam HR Raman system using a 532nm wavelength laser at a power of 0.7 mW to characterize all the materials seen in this thesis.

### 3.2 Electronic Transport Measurements

The electronic transport properties of materials are measured by the 2-terminal, 3-terminal, and 4-terminal device configurations. Basic 2-terminal devices are measured by contacting 2 electrodes onto the material, a source electrode and a drain electrode. A Keithley 2400 is used to apply a voltage bias to the source electrode and the other being the drain. This will induce a current in the material and allow for the measuring of the device's resistance. The problem with a 2-terminal measurement is that it will include contact resistance between the electrodes and material both at the source and drain electrodes. This can be measured using 3-terminal measurements (see figure 3.2). This technique uses a 3rd electrode which can either be between the source and drain electrodes or outside. This 3rd electrode is connected to an electrometer with high impedance (~$10^{11}$ Ω) and, depending on the configuration, can measure the voltage drop across the contact electrode. Using Ohm's law, the contact resistance can then be calculated.

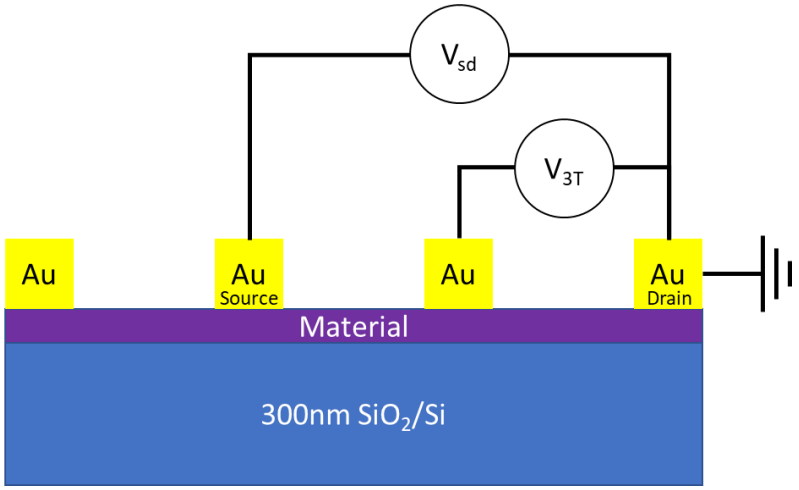


**Figure 3.2:** Standard illustration of a 3-terminal measurement to accurately measure the contact resistance of the electrode.

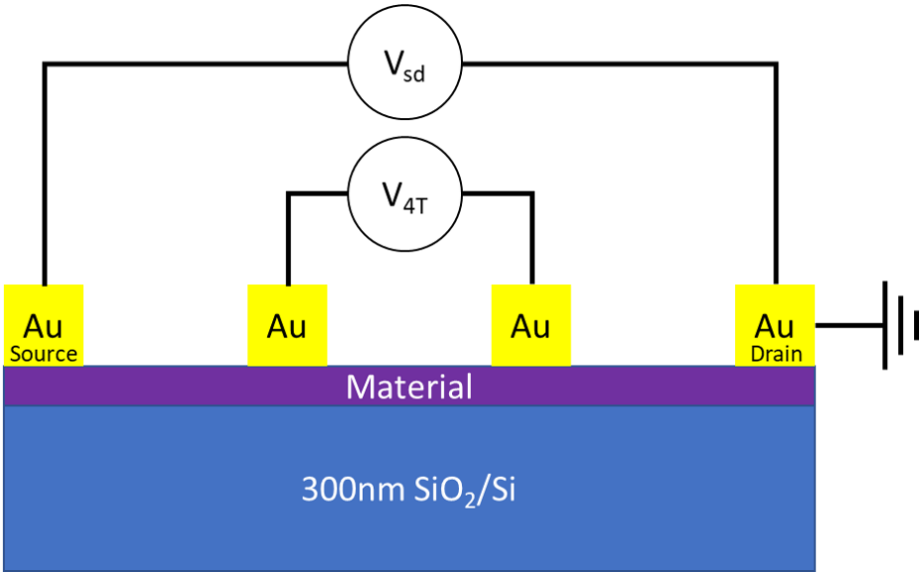


**Figure 3.3:** Standard illustration of 4-terminal measurement to accurately measure a materials resistance sans contact resistance.

The 4-terminal measurement uses 4 electrodes configured so that two electrodes are situated in between the source and drain electrodes with both electrodes being connected to a voltmeter (see figure 3.3). When a bias is applied between the source and drain the electrometers will measure the voltage at each electrode. Subtracting the voltage difference and again using Ohms law the resistance can be measure but this time the calculated value is the materials resistance devoid of any contact resistance and therefore is the most accurate measurement of a material's inherent resistance.

### 3.3 Atomic Force Microscopy

Atomic Force Microscopy (AFM) is a technique that allows the measuring of topical features at the nanoscale down to the angstrom ($\sim 10^{-10}$ m) level. The main principle of AFM is based off of Hooke's law and the vibrational frequency of the probe tip as it interacts with the surface of the material. This technique can be performed in two ways, contact and noncontact mode. In contact mode the tip is dragged across the surface of the sample and when the laser deviates from the designated origin the z-axis stage moves up or down to return the laser to the original position and by measuring this change the instrument can map out a topography of the sample. The downside of this contact mode is that it only works well on hard surface samples. For this reason, we use the noncontact or tapping mode" to measure all of the samples in this thesis. Noncontact mode relies on the frequency of the tip oscillation

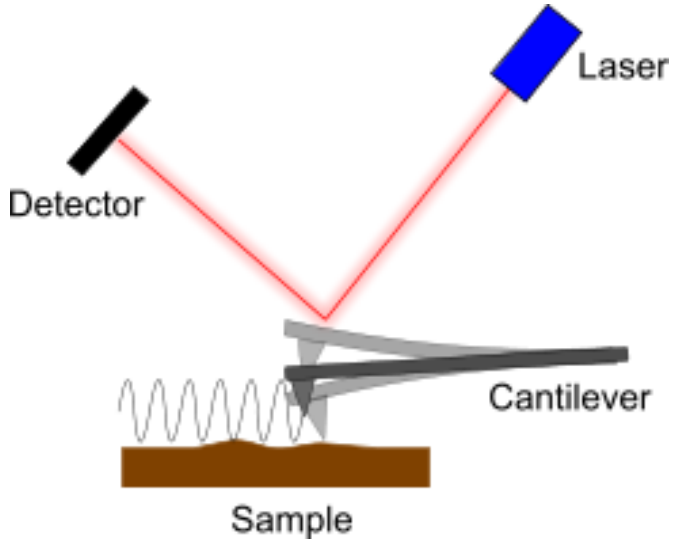


**Figure 3.4**: Atomic force microscopy illustration of the tip scanning a samples surface[78]

The probe vibrates with a particular frequency and by measuring the change in the probes movement, again using a laser focused on the head of the probe, the surface of the sample can be imaged however this time instead of adjusting the z-axis height, the change in position of the laser by the detector will be used to map out the sample. This mode is advantageous because it can measure surfaces that have softer materials such as transition metal di or tri chalcogenides. The corresponding change in height determines the materials thickness which gives information about the material such as the number of layers of a 2D material, the thickness of a single layer of 2D material, and to some degree the cross-sectional area for a 1D nanorod.

### 3.4 Chemical Vapor Deposition

Chemical vapor deposition (CVD) is a common research synthesis method due to its simplicity. Unlike chemical vapor transport where an ampule is evacuated and sealed with,

usually, a halogen carrying gas, CVD is an “open” system whereby the quartz tube is flowing an inert gas such as argon or nitrogen through the tube and into a bubbler that allows for the tube to be “closed” via a water seal effectively acting as a one way valve for the gas to flow. This quartz tube is placed in a tube furnace which can be controlled to ramp anywhere from ambient to 1200°C if so desired. The gas flow is controlled by flowmeters to regulate the rate at which gas flows through the tube.

CVD is also a preferred method of synthesis due to the fact that one can use any type of chemical reagent solid, liquid, and/or gas but also any type of substrate for the single layer or multi-layered material to grow from amorphous mediums to highly crystalline while not being beholden to lattice matching or chemical restrictions.


**Figure 3.5**: Image of a chemical vapor deposition system consisting of a 1) tube furnace 2) quartz reaction tube 3) exhaust bubbler and 4) temperature controller

### 3.4.1 $MoTe_2$ Grow Process

The growth of $MoTe_2$ begins by weighing out 7 mg of molybdenum trioxide powder into an alumina combustion boat, see Figure 3.6. In a second boat 16 mg of elemental tellurium powder is add. The 300 nm $SiO_2$/Si substrate is placed $SiO_2$ side down on top of the molybdenum trioxide containing boat[79-81] so that it is half covering the top of the boat. The boat and substrate are carefully loaded into a 1" diameter quartz tube situated in the tube furnace and placed in the center of the furnace heating element. The second boat containing the tellurium powder is placed 3" away from the center boat upstream of the process gas flow direction.


**Figure 3.6:** Alumina combustion boat from Coorstek 3x1 cm.

The tube is then closed. The growth process proceeds with a purging step by adjusting a flow meter valve to flow argon gas at a rate of 0.5 standard cubic feet per hour (SCFH) for 10 minutes displacing any oxygen from the tube. After the purge comes a two-step ramp: the first is a ramp from ambient temperature, 20°C to 500°C over 20 min with the argon gas flow decreased to 0.1 SCFH. During the second ramp step the furnace is ramped from 500°C to 680°C over 20 min under the same argon gas flow rate. Once the furnace reaches

680°C the hold step occurs whereby the furnace is held at this maximum temperature for 15 minutes maintaining the argon gas flow at 0.1 SCFH and opening a second flow meter to add in hydrogen gas to the process gas flow at 0.05 SCFH and if the 1T phase is the desired phase then another process gas, carbon dioxide, is add to the argon and hydrogen gas flows at 0.05 SCFH flow rate.

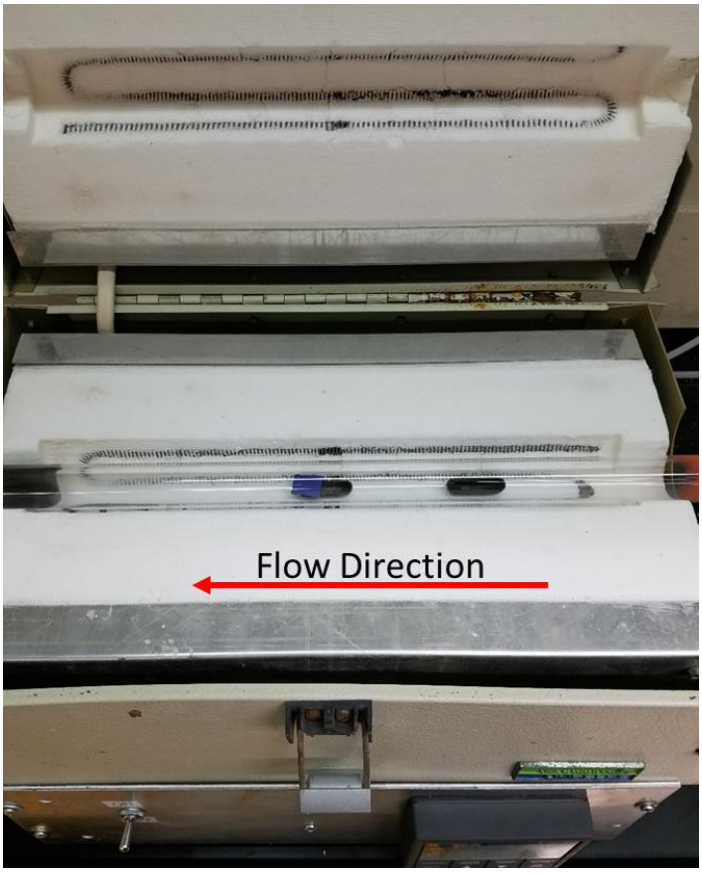


**Figure 3.7:** $MoTe_2$ growth set up with molybdenum oxide boat at the center of the furnace and the tellurium boat positioned up stream of the flow to reach max volatility when the furnace is at the maximum hold temperature

If the desired phase is the 2H or 1T' then the carbon dioxide gas is not introduced. After the hold step there is a two-step cooling process: the first is a 20 minute cool from 680°C

down to 500°C with the process gases remaining the same for the first 10 min of the cool when the hydrogen gas is turned off (and the carbon dioxide if growing the 1T phase) leaving only the argon flowing at 0.15 SCFH for the last 10 minutes before turning off the power to the furnace. The second cooling step comprises of opening up the clam shell type tube furnace with a fan place toward the center of the tube to cool it down to ambient temperatures at differing rates depending to the desired phase: for 1T it is opened at 500°C, for 1T' then it is opened below 300°C, and for the 2H waiting until the furnace has cooled naturally to below 100°C.

### 3.4.2 $TaSe_3$ Growth Process

The growth of $TaSe_3$ occurs in the same 1" diameter clam shell type tube furnace as the $MoTe_2$ process described above. Into an alumina boat 50 mg of tantalum pentachloride ($TaCl_5$) (99.99%, Sigma Aldrich) crystals are weighed and carefully ground to make a fine powder. In a second boat 50 mg of elemental selenium powder (99.99%, Sigma Aldrich) is added. In the boat containing it the tantalum chloride, 130 mg of diethyl ether ($OEt_2$) is added to form the adduct ($TaCl_5[OEt_2]$) and mixed while adding the selenium content of the second boat before the mixture naturally dries. An additional 50 mg of selenium is added to the, now empty, secondary boat. Once the tantalum chloride-ether adduct and selenium containing boat has dried 150 mg of ethanol (EtOH) is added and mixed well to solvate the solid precursor mixture. The mixture is then placed onto a 65°C hotplate to drive off excess solvent until the mixture has the consistence of a slightly runny tar and removed from the heat. A 300 nm $SiO_2$/Si substrate is placed $SiO_2$ side down on top of this boat leaving a slight amount of space on either side of the boat and placed

carefully in the quartz tube at the center of the furnace. The second boat containing the selenium is placed 1.5” away from the center boat upstream of the gas flow direction. The furnace is purged with argon at a flow rate of 0.5 SCFH for 10 minutes. After the purge the furnace is ramped to 400°C over 15 minutes with a flow rate of argon at 0.1 SCFH.

During the ramp at 200°C hydrogen gas is introduced at 0.05 SCFH. Once the furnace reaches 400°C it is held for 3 minutes with the same flow rate of argon and hydrogen after which the hydrogen is turned off, the flow rate of argon is turned up to 0.15 SCFH and the furnace is turned off and opened with a fan to cool the furnace back to ambient temperature over 15 minutes.

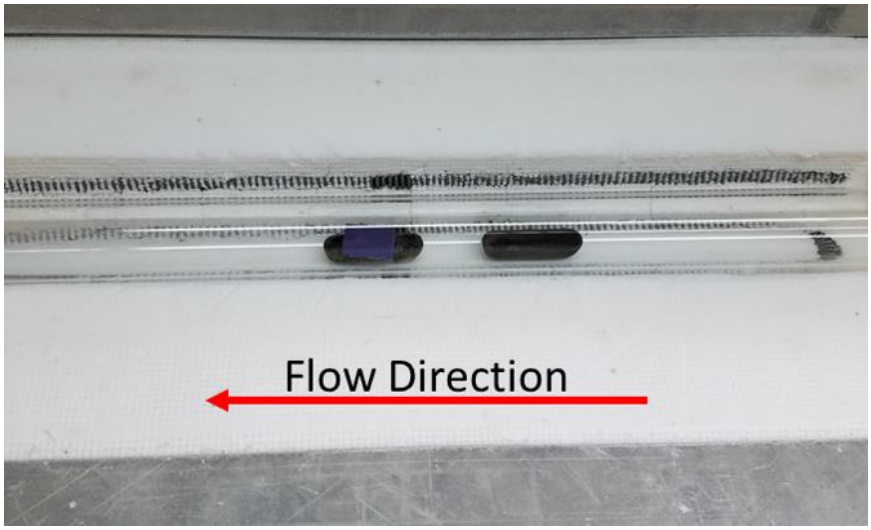


**Figure 3.8:** $TaSe_3$ growth process boat positioning with the substrate placed in the center of the combustion boat containing the tantalum adduct and selenium mixture with the secondary selenium powder boat upstream.

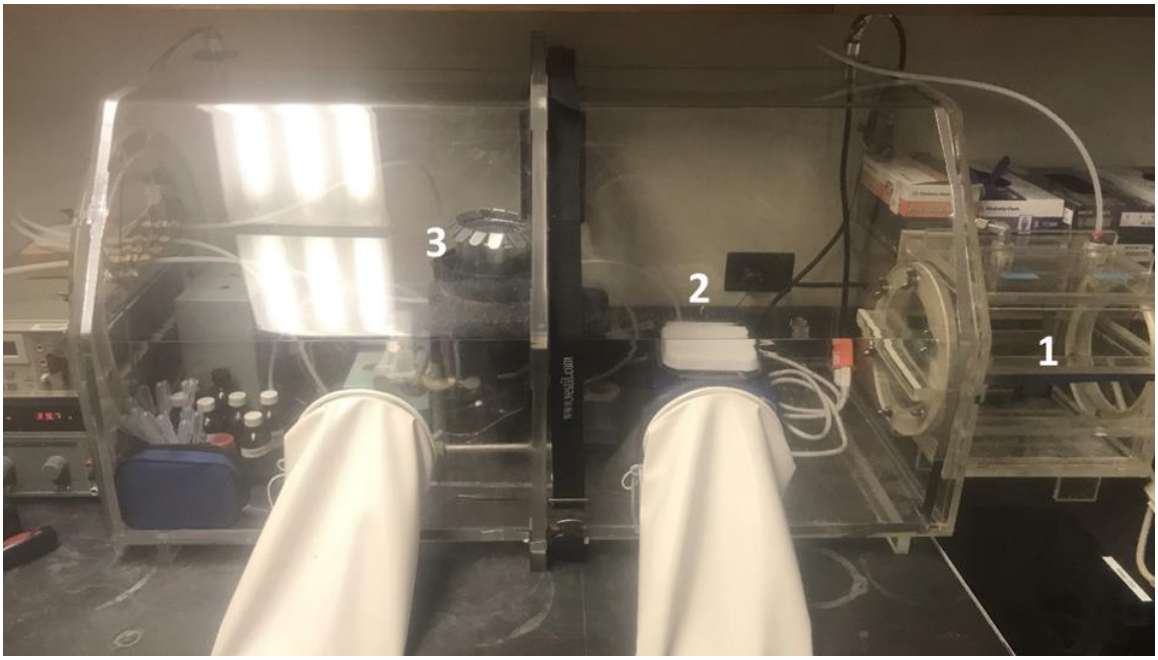


**Figure 3.9:** Glovebox used for spin coating of the TMD and TMT samples showing 1) load lock, 2) the hotplate used to bake the samples at 150°C for 1 minute, and 3) the spin coater that spins the sample at 4000 rpm for 1 minute to spread an even layer of PMMA on the sample

# Chapter 4: Results

## 4.1 Molybdenum Ditelluride, $MoTe_2$

The following chapter contains excerpts from "Chemical Vapor Deposition Growth of Few-Layer $MoTe_2$ in the 2H, 1T′, and 1T Phases: Tunable Properties of $MoTe_2$ Films" by T.A. Empante, et. al.[82]

Cooling of the CVD furnace proceeds in three steps: initially the furnace temperature is ramped down from the maximum temperature to 600°C over 10 minutes at equal flow rates $H_2$, $CO_2$, and Ar for a total of 0.15 SCFH. The use of $CO_2$ is motivated by Ref.[47] because density functional theory calculations suggest that it has the potential to stabilize the T-type phases over the 2H phase of $MoTe_2$. The second step ramps the furnace down from 600°C to 500°C in 20 min under a flow of 0.1 SCFH of Ar; $H_2$ and $CO_2$ flow is terminated. After the end of the second step the furnace power is turned off. The 2H phase is dominantly attained by leaving the clam shell closed until the furnace temperature is below 100°C. The 1T' phase dominantly results by opening the clam shell as soon as the furnace cooled to 350°C. Finally, the 1T phase is dominantly obtained, if the clam shell is opened at 450°C. As soon as we open the clam shell the process tube is cooled directly by a fan. Fig. 4.2 shows Raman spectra and optical micrographs of the $MoTe_2$ films in all three phases. The growth procedure differs only by the cooling rate – and the formation of 1T phase films requires the presence of $CO_2$ in addition to $H_2$. While we can obtain extended (>10 μm) single-layer films of 2H $MoTe_2$, we find the growth of uniform single- or few-layer thickness films of 1T and 1T' $MoTe_2$ to nucleate frequently in a circular

fashion around growth seeds. Fig. 4.2 also shows atomic force microscopy profiles revealing the layer thickness of our $MoTe_2$ samples. CVD growth of molybdenum and tungsten disulfides and diselenides reliably leads to triangular islands with straight edges in our lab.[80, 81] In contrast, $MoTe_2$ films generally do not adopt straight edges, so that the edge shape cannot be used to indicate crystallographic orientation. The highest propensity for straight edges we find for 1T $MoTe_2$. We discuss the origin of this phenomenon below.

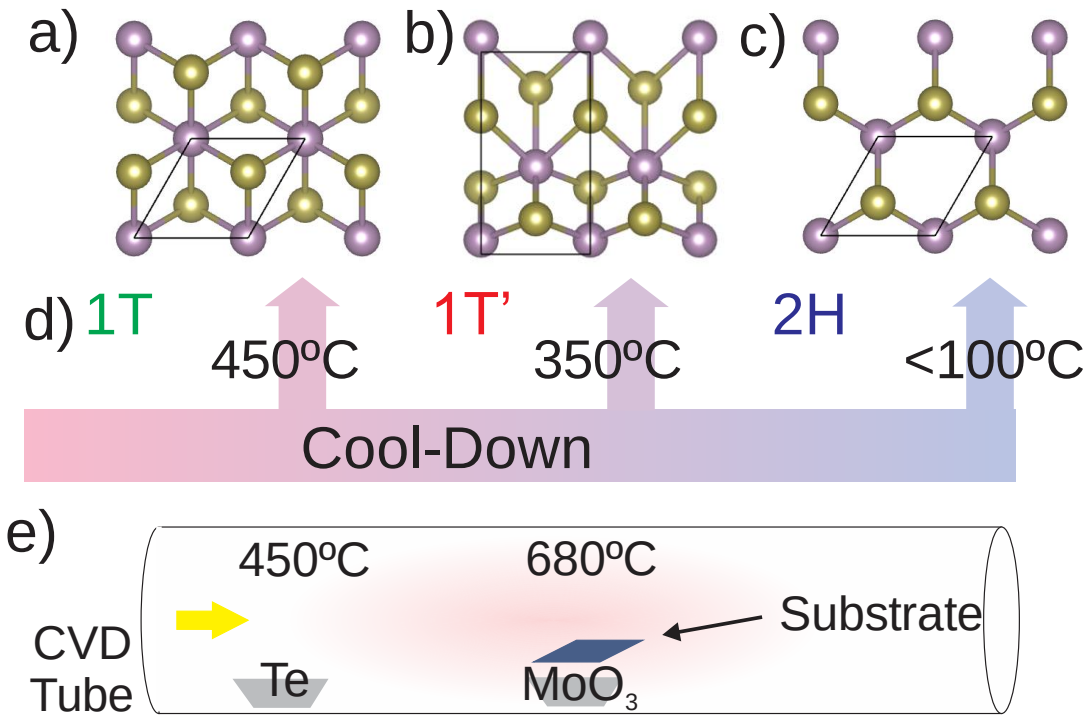


**Figure 4.1:** $MoTe_2$ Phases and Overview of Preparative Technique a,b,c) top view onto a sheet of 1T, 1T' and 2H $MoTe_2$, respectively. The unit cells are indicated. d,e): CVD growth of few-layer $MoTe_2$ in a tube furnace. The temperature (indicated) at which the growth is quenched determines the resultant $MoTe_2$ phase.

Microscopy profiles revealing the layer thickness of our $MoTe_2$ samples. CVD growth of molybdenum and tungsten disulfides and diselenides reliably leads to triangular islands with straight edges in our lab.[80, 81] In contrast, $MoTe_2$ films generally do not adopt straight edges, so that the edge shape cannot be used to indicate crystallographic orientation. The highest propensity for straight edges we find for 1T $MoTe_2$. We discuss the origin of this phenomenon below.

Density functional theory (DFT) based structural minimization finds both the 2H and 1T structure as local minima of the energy, if a 1x1 crystallographic cell is utilized. The 1T structure has a lower (unfavorable) binding energy per stoichiometric unit of 0.51eV/f.u.. If a 2x1 supercell is used, no local energy minimum at the 1T phase is detected; rather the 2H and 1T' phase are found and the latter has a binding energy lower (unfavorable) by 0.03 eV/f.u..

We calculated the phonon spectrum for each structure by means of 3x3 supercell; while neither the 2H nor the 1T' exhibited negative phonon frequencies, a band of negative frequencies was found for the 1T structure when expanded to a 3x3 supercell. This indicates that this phase requires stabilization by extrinsic effects that will be discussed in the following section.

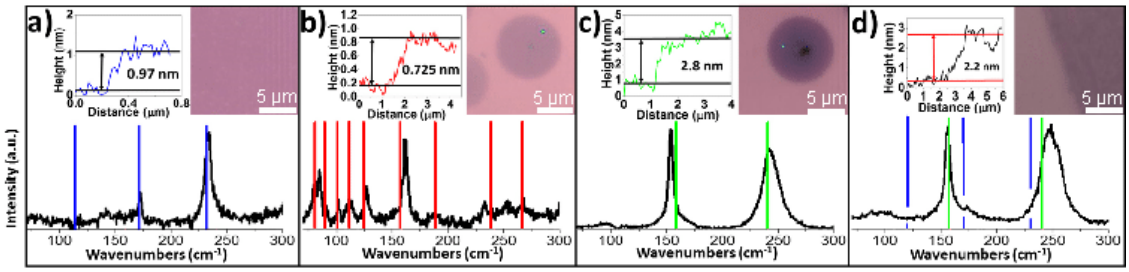


**Figure 4.2:** Comparison of the experimental (black) Raman spectra for each phase of $MoTe_2$ with computational predications (colored lines): a) 2H continuous film, b) 1T' island, and c) 1T island. d) mixed phase film as indicated by the presence of 2H Raman peaks in an otherwise 1T film. The AFM line scans indicate the film thickness.

Raman spectroscopy is used to identify and characterize the $MoTe_2$ phases. Samples not quenched during the growth process exhibit Raman peaks at $171cm^{-1}$ and $233cm^{-1}$, as shown in Fig. 4.2a. These features agree well with peaks predicted from DFT calculations of the 2H phase at $170cm^{-1}$ and $230cm^{-1}$, at a deviation of 0.59% and 1.30%, respectively. Our values also corroborate published results on exfoliated[36, 38-43] and CVD-grown[44-46] 2H:$MoTe_2$.

Quenching at ~350°C leads to an $MoTe_2$ film (Fig. 4.2b) that exhibits a number of Raman features that are typically associated with the 1T' phase of $MoTe_2$. Because of the expanded supercell and lower symmetry of this structure, the set of Raman-active modes is wider. In particular, we observe pronounced features at $80cm^{-1}$, $85cm^{-1}$, $102cm^{-1}$, $112cm^{-1}$, $126cm^{-1}$, and $162cm^{-1}$. These match our DFT predictions within an error of 1.25%, 4.49%, 2.00%, 0.90%, 1.61%, and 3.18%, respectively. The Raman modes observed in these films also correspond well to literature values.

Quenching the film growth at 450°C, we observe a Raman spectrum that is clearly distinct from the 1T' phase (panel c). It is significantly simpler consisting of two prominent modes only at 155cm$^{-1}$ and 242cm$^{-1}$, each of which is slightly broader than is counterpart in the 2H phase. Comparison to our computational work reveals good agreement of the two experimental Raman modes with the Raman modes of 1T $MoTe_2$, which we predict at 159cm$^{-1}$ and 240 cm$^{-1}$ respectively. Based on this finding, we assign this phase to be 1T $MoTe_2$. We note that the higher-energy mode is consistently broader in the spectral signature. We are not aware of prior experimental observation of this phase.

On the Mechanism of Phase Control: We interpret the ability to grow three different phases of $MoTe_2$ by procedures that differ only during the cooling process as an indication that during initial growth, $MoTe_2$ occurs in the 1T phase. A number of reports suggest thermodynamic preference for the octahedral (1T-type) phase at elevated temperatures for a number of TMD materials; for instance, for $TaS_2$ an unreconstructed 1T phase has been observed.[83] We find that in the absence of both $H_2$ and $CO_2$ during growth, we cannot obtain 1T $MoTe_2$; in prior computational work we have shown that both H and $CO_2$ adsorption reduce the energy difference between the H and T' structures, potentially reducing the bias of the growth toward the H phase.[47] While these calculations motivated our choice of gases to include during growth, the actual role and specific bonding of these gases may differ from the assumptions made in the survey of Ref. [47] . We hence attribute the initial growth in the 1T phase to the interplay between $CO_2$, $H_2$, (and possibly the underlying $SiO_2$ substrate) with the emergent $MoTe_2$ film.

Fig. 4.3 shows the free energy for each phase as a function of temperature; the lowest phase at each temperature is the thermodynamically preferred one. At low temperatures this is the 2H phase and it transitions to the 1T' phase at ≈310°C. The prediction of the transition temperature between the 2H and 1T' phase neglects effects of gas-phase species and substrate interactions. The computed value of 311ºC is in good agreement with the experimental observation that we need to start quenching at ≥350ºC so as to avoid the 2H phase. Unfortunately, computational modeling of the 1T phase would require precise knowledge about the high-temperature chemical interplay that stabilizes it, which is beyond our computational capabilities. As a zeroth-order approximation we assume the adsorbate interplay to shift all negative phonon density to the lowest positive phonon frequency of 1T $MoTe_2$. This crude approach is conceptually motivated by the assumption that weak adsorption of the gas species – and weak binding to the substrate – is necessarily associated with soft vibrational modes. However, we emphasize that this approach does not represent an authentic representation of the system – and that the resultant computational transition temperature at 916ºC should not be interpreted quantitatively. Conceptually, this approach leads to a consistent explanation of our experimental results, in as much as it predicts thermodynamic stability of 1T $MoTe_2$ at the highest temperatures, followed by preference for 1T' and 2H at successively lower temperatures. Consequently, if starting at sufficiently high temperatures the growth is quenched rapidly enough, one obtains 1T $MoTe_2$. As the temperature is gradually reduced while $CO_2$ and $H_2$ are purged out of the tube (as we only flow them at the peak temperature of the growth), the 1T' becomes thermodynamically stable and it will be the final product,

if the growth is quenched in the correct temperature regime. Finally, if the film is brought gradually all the way down to near room temperature, then the thermodynamically preferred phase at room temperature, namely 2H, emerges.

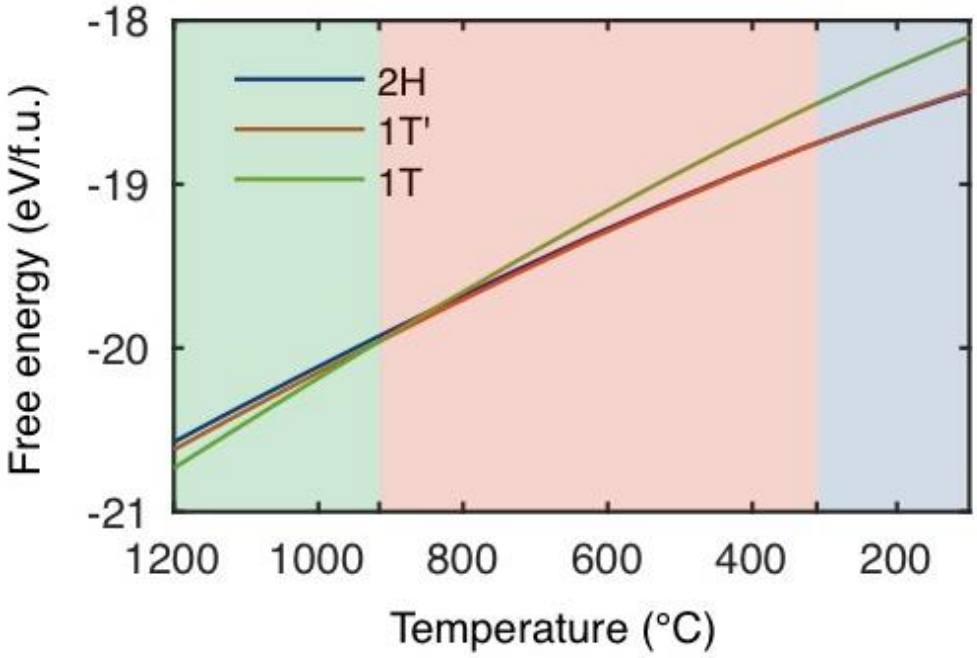


**Figure 4.3:** Computed phase stability: Free energy of $MoTe_2$ in the 2H, 1T' and 1T phase based on calculations of the phonon density of states in the three phases. The curve for 1T $MoTe_2$ is subject to the limitations described in the text. At each temperature, the curve with the lowest free energy represents the thermodynamically preferred phase. Spin-orbit coupling effects are included in the underlying electronic structure calculations for all phases. Relaxed lattice constants are used for all phases.

The assumption of phase transitions during cooling of the $MoTe_2$ film suggest the highest propensity for straight edges in 1T $MoTe_2$ and successively lower definition of the mesoscopic crystallographic order in 1T' and 2H $MoTe_2$, as these films had to undergo

reorganization in the course of their phase transitions from the growth phase. Our observations affirm this prediction.

We investigated whether the presence of $CO_2$ during growth leads to incorporation of carbon into the $MoTe_2$ film. X-ray photoelectron spectroscopy (XPS) measurements confirm that only comparatively small amounts of carbon are present after the growth is complete. Raman spectroscopy also shows the absence of an amorphous carbon film. The incorporation of small amounts of oxygen in the final film can unfortunately not be determined in this way because of the abundance of oxygen in the $SiO_2$ substrate and the $MoO_3$ precursor.

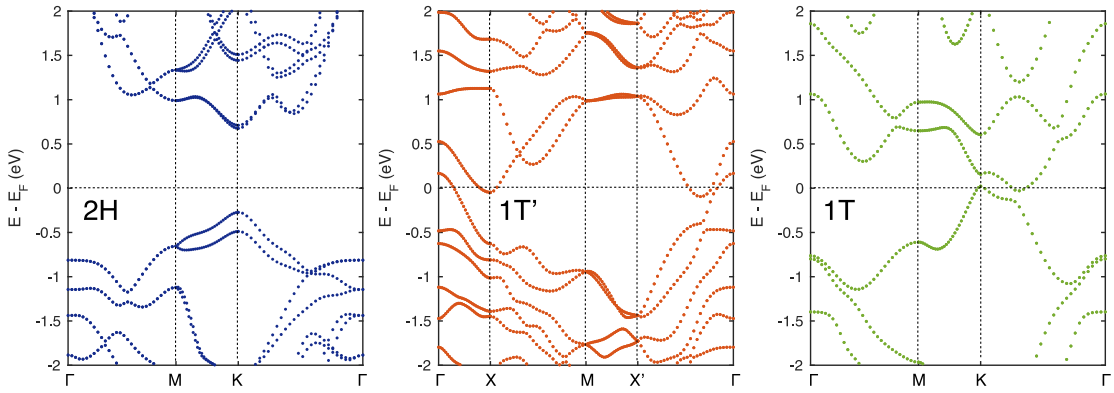


**Figure 4.4:** Band structures calculations of monolayer films: Left semiconducting 2H-$MoTe_2$, center metallic 1T'-$MoTe_2$, and right semimetallic 1T'-$MoTe_2$. Spin-orbit coupling effects are included in all calculations.

Band Structure and Semimetallicity: Figure 4.4 shows on the right the band structure of 1T $MoTe_2$ and compares it to the one of the 2H (left) and 1T' (center) phase. 1T $MoTe_2$ is metallic; an electronic feature resembling a valence band crosses the Fermi

level at the K point by a very small amount; a feature resembling a conduction band crosses below the Fermi level by a similar, very small amount at a low-symmetry point along Γ-K. The amount of Fermi level crossing is less than 50 meV in each case and does not exceed the expected accuracy of DFT calculations leading us to classify this material as a potential semimetal.

We validate the predicted properties of 1T $MoTe_2$ by electrical transport measurements on all three phases. For contacts we utilize Sc/Au stacks fabricated by electron-beam lithography. Fig. 4.5a shows the results obtained on 2-terminal devices. The 2H device of channel width/length of 2.4 μm/0.8 μm used 1L material; the 1T' devices of 3.5μm /1μm used 1L material; the 1T devices of 25 μm/0.5 μm used 1L material. It is well established that 2H $MoTe_2$ exhibits the properties of a semiconducting film including comparatively low conductivity as well as a ready response to an applied bottom gate. Our measurements corroborate this showing a resistance of 570 MΩ at zero gate and $V_{SD}$=0.5V corresponding to a resistivity of 168 Ω cm. Our film shows a mobility μ of 0.03 $cm^2$/Vs under gating through 300nm of $SiO_2$, in line with prior work on CVD films.[40, 45, 84]

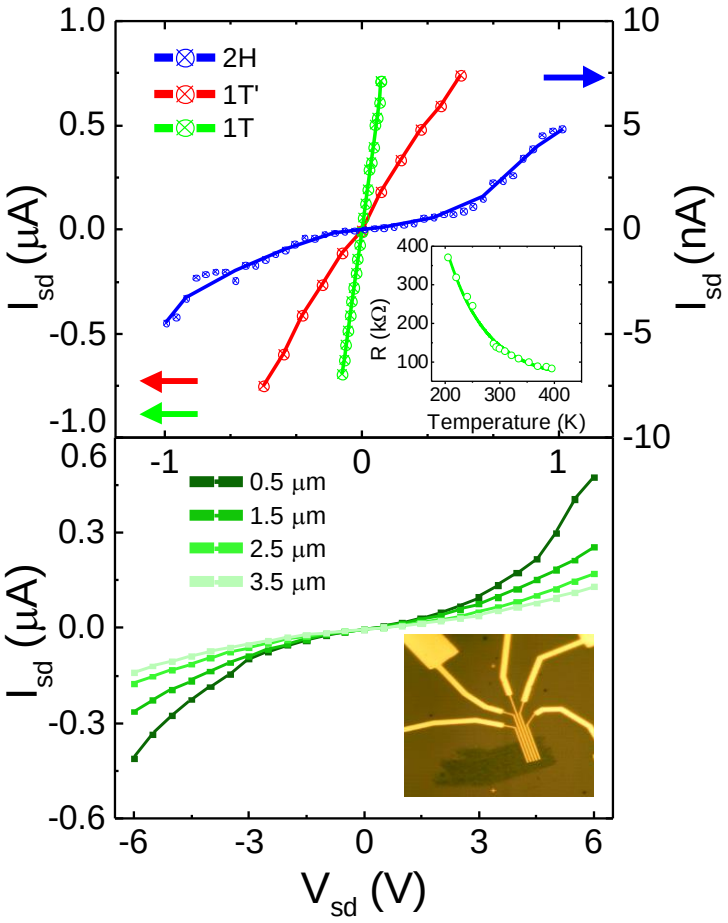


**Figure 4.5:** Transport Measurements: a) source-drain current $I_{SD}$ as a function of source-drain voltage $V_{SD}$ across two-terminal devices fabricated on the $MoTe_2$ materials of Fig. 14: 2H $MoTe_2$ (blue, right y-axis) exhibits *p*-type semiconducting behavior. 1T' (red) and 1T (green) show metallic, ohmic behavior and significantly increased currents (left y-axis) that correspond to resistances of 0.67 MΩ and 0.14 MΩ, respectively. The inset shows the temperature-dependence of the resistance of a 0.5 micron channel of 1T $MoTe_2$ measured in a 4-probe setup. b) $I_{SD}$-$V_{SD}$ curves as a function of channel length (measured electrode center to center) for a $MoTe_2$ device with a mixture of 1T and 2H phases: the response is semiconducting despite the low Raman contribution of the 2H phase.

The 1T' phase reveals metallic behavior with electrode-to-electrode resistances in the upper kΩ regime. For the 1T material we find an electrical response with significant sample to sample variation (see below); the conductivity of few-layer 1T $MoTe_2$ films can exceed that of our best single-layer 1T' devices. The resistivities of the 1T and 1T' phases of Fig. 4.5 are 2.0 Ω cm and 0.17 Ω cm, respectively. Neither the 1T nor the 1T' devices of Fig. 4.5a show an appreciable response to back gating. However, the 1T phase exhibits a decreasing resistance with temperatures (inset of Fig. 4.5a) as expected for a semimetal.

Hybrid Phase Films: Slight variation in the $MoTe_2$ growth parameters, such as the temperature or the rate at which the quench occurs, results in uniform films that exhibit Raman spectra of a combination of two (or all three) $MoTe_2$ phases within a diffraction limited sample spot. We have observed every which pairing and focus in the following on a device that combines the 1T and 2H phases.

The Raman spectrum and micrograph of such a film is shown in Fig. 4.2d. The film is 3 layers thick and the Raman spectrum is practically constant across the entire film region. Fig. 4.5b shows the transport properties between electrodes at successive separation (see inset for device image); a linear fit results in a contact resistance of 17 MΩ (or 0.75 $\Omega cm^2$) and a channel resistance of 14 MΩ/μm (or 2.7 Ωcm). 4-point configuration resistance measurements agree with the ones obtained here.

1T $MoTe_2$ has a significantly stronger Raman response than the 2H material. Despite the dominant 1T character of the material's Raman spectrum, the device exhibits

a semiconducting behavior and responds to gating just like the 2H phase, yet the total conductivity exceeds that of our 2H $MoTe_2$ devices by two orders of magnitude while lacking by a similar factor compared to the pure 1T device. This finding suggests that judicious tuning of the 1T-2H mixture allows tailoring the conductivity and gate-response of $MoTe_2$-based devices at will.

Sample Characterization & Device Fabrication: Sample characterization proceeded on a Horiba LabRam system for imaging and using a 532 nm laser for Raman spectroscopy. Atomic force microscope (AFM) was performed on a Veeco Dimension 5000 system with samples capped in PMMA for environmental stability. Transport measurements proceeded in a probe station housed in a glove box utilizing a Keithley 2400 source meter.

Fabrication of contacts for electrical transport measurements involved e-beam lithography on a Leo SUPRA 55 electron microscope. A double stack of MMA (EL9)/PMMA (A4) served as resist; development occurred in a 1:3 mixture of methyl-isobutylketone and isopropyl-alcohol. Immediately subsequent, we deposited 6-10 nm Sc followed by 80-100 nm Au in an e-beam evaporator (Temescal BJD 1800). Lift-off was performed in acetone.

Computational Method: Our computational work uses density functional theory (DFT) as implemented in the Vienna *Ab Initio* Simulation Package (VASP)[85, 86], using the Projected-Augmented Wave (PAW) method[87]. Electron exchange and correlation effects were treated with the generalized gradient approximation (GGA) functional of Perdew, Burke, and Ernzerhof (PBE)[88]. Spin-orbit coupling effects were included for non-

vibrational calculations. A plane-wave basis set with a kinetic energy cutoff of 350 eV was employed. We sampled the Brillouin zone using an 18×18×1 Monkhorst-Pack[89] k-point grids. The computational cell is 16 Å along the interlayer direction. A rectangular unit cell with two formula units of $MoTe_2$ was used for 2H and 1T' phase, and a hexagonal unit cell with one formula unit of $MoTe_2$ was used for 1T phase.

### 4.2 Tantalum Triselenide, $TaSe_3$

The following chapter contains excerpts from "Low Resistivity and High Breakdown Current Density of 10-nm Diameter van der Waals $TaSe_3$ Nanowires by Chemical Vapor Deposition" by T.A. Empante, et. al.[90]

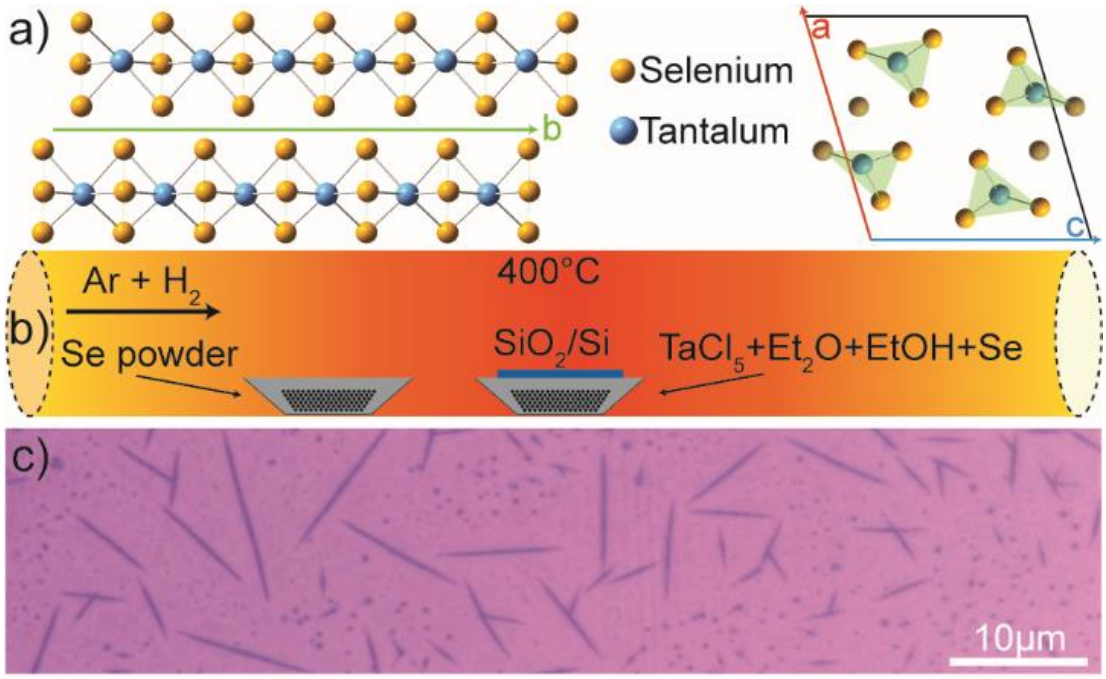


**Figure. 4.6** a) Crystallographic structure of $TaSe_3$ consisting of four nanowire $TaSe_3$ stacks per unit cell along the b axis. The greyed atoms inside the unit cell correspond to those shown outside of it in order to highlight the selenium triangles between each tantalum plane; b) schematic representation of the chemical vapor deposition process inside a tube furnace; c) optical image of a population of $TaSe_3$ nanowires.

This manuscript focuses on the preparation and characterization of a specific transition metal trichalcogenide (TMT), $TaSe_3$, on a commercial 300 nm $SiO_2$/Si substrate

using process parameters (ambient pressure, ≤ 400°C process temperature, ≤ 5 min process duration) that are amenable to conventional back-end-of-the-line (BEOL) process limits. Despite the large interest in TMDs, TMTs have been largely left unstudied at the nanoscale; they have varying structures from 2D thin films to 1D wires and properties ranging from insulating to metallic.[49, 50, 68, 91] $TaSe_3$ has a monoclinic unit cell and consists of stacks of Ta atoms, each of which are bonded to three selenium atoms above and below along the b axis (Fig. 4.6a). Neighboring -Ta-$Se_3$-Ta-$Se_3$- stacks are separated from one another by a tubular vdW gap exposing chalcogen atoms only, similar to the gap between the Se-Mo-Se layers in 2D $MoSe_2$. $TaSe_3$ has been known for a long time and bulk samples have been prepared using chemical vapor transport (CVT), a process that requires long process times and is not amenable to current semiconductor processing paradigms; exfoliation of such samples yielded the results reported by some of us earlier.[66-68]

Interconnect performance is crucial for low-power high-clock-frequency computing: the transition from aluminum to copper interconnects starting some 20 years ago was driven by both the better conductivity of copper and the better manageability of electromigration in copper, the key failure mechanism for interconnects.[92, 93] However, as the cross section of an interconnect becomes shorter than the electron mean free path (~40 nm in copper),[70-72] its resistivity increases dramatically due to scattering at the material surface and at internal grain boundaries. A 1D material without surface dangling bonds or internal grain boundaries would, in theory, lack these drawbacks and be a prime candidate.

The best aspect ratio of interconnect cross sections has been studied intensely optimizing interconnect topology while reducing capacitive cross coupling. Modern

processors use aspect ratios between 1.2 and 1.5 on the first four (0-3) metal layers.[94] We show a CVD method that natively generates nanoscale wires with a width to height aspect ratio of ~1, close to the optimal one.

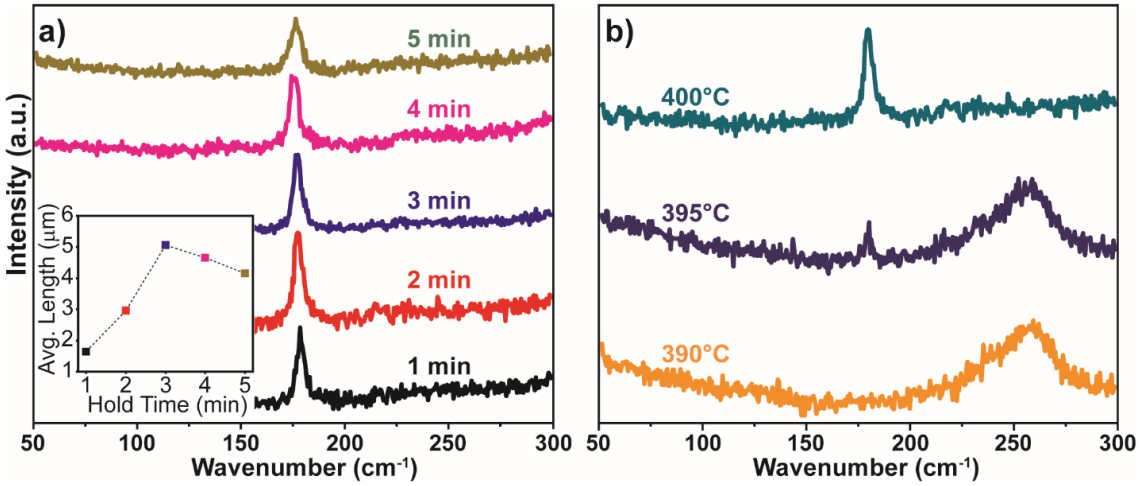


**Figure 4.7:** a) Raman spectra of $TaSe_3$ nanowire bundles held for different duration at the growth temperature of 400°C. A hold time beyond 3 minutes causes the Raman spectrum to broaden. The inset shows the resulting length distribution peaking at 3 min hold time; b) Nanowire Raman spectra as a function of growth temperature. Starting at 400 °C the desired peak at ~180 $cm^{-1}$ is dominant.

Raman spectroscopy (Horiba Labram HR800, 532 nm wavelength laser, linear polarization, 0.8 mW of laser power on sample) was used to characterize the nanowire bundles grown at hold times varying from 1 to 5 minutes (Fig. 4.7a) at 400°C. The feature at ~180 $cm^{-1}$ is typically referred to as B2 or B2/Ag in the literature. In addition, if we align the plane of polarization of the Raman excitation perpendicular to the nanowires, we find a second, weaker mode at ~ 215 $cm^{-1}$. This peak in the literature referred to as another A1g

mode. Computational modeling of the phonon spectrum and the associate atom displacement suggest that the dominant mode in Fig. 4.7a is associated with axial wagging of the selenium trimer with regards to the Ta atom and the peak at ~ 215 $cm^{-1}$ with the symmetric and asymmetric stretch motion of the Se atoms in the trimer. The supporting information provide angle-dependent Raman spectra and graphic representations of the modes. The supporting while nanorods were formed in each instance, up to ~3 minutes hold produced the nanowires with the sharpest Raman signature at ~180 $cm^{-1}$; longer hold is associated with a broadening of the Raman mode by a higher energy shoulder. The supporting material shows a table of the fit parameters of the spectra. Determining the average length of a large set of nanowires generated at each hold time using optical microscopy, we find a maximum wire length at ~3 min hold time (inset in Fig. 4.7a). The supporting material shows histograms. This finding suggests that during the hold time the nanowires do not only form and elongate, but also can decompose, presumably from selenium loss. We studied the Raman spectra of the nanowires as a function of the peak process temperature (Fig. 4.7b) and find that 400°C is the minimum temperature at which nanowires with the desired Raman signature form. The nanowires with the broad spectral feature at ~260 $cm^{-1}$ formed at process temperatures below 400°C exhibit transport properties far inferior to those nanowires described in the remainder of this manuscript; their precise composition is unknown to us.

In order to be of technological relevance, the $TaSe_3$ 1D vdW nanowires need to be prepared on the scale of a few nanometers in cross section yet significant in length. To this end we evaluated the length to width to height ratios in a population of nanowires. Fig.

4.8a and b show atomic force and scanning electron microscopy (AFM and SEM, respectively) images of the same population of growth seeds and short wires. We obtain the nanowire height from atomic force microscopy yet we use SEM to establish the nanowire width because of the finite size of any AFM tip and associated convolution of tip radius and nanowire width. Fig. 4.8c shows the width-to-height aspect ratio of the nanowires plotted as a function of the nanowire length. Nanowires shorter in length than ~120 nm exhibit ratios between 0.75 and 2.5 which we attribute to the seeding of the growth (gray area). Longer nanowires have an aspect ratio very close to unity: as the axial growth sets in, the nanowires appear to minimize surface area by maintaining a width to height ratio near unity (black markers). Fig. 4.8c includes also a significant number of long nanowires that form the basis of the transport measurements in the next section of this manuscript. The inset shows the dependence of width to height for the black markers of the main panel. The slope is 1.06.

For measurement of the electrical transport properties of the $TaSe_3$ nanowires we employed electron beam lithography (EBL) to fabricate contacts consisting of 5 nm of yttrium for adhesion and 50nm of gold for conduction and stability. Previous studies of $TaSe_3$ nanowires[66-68] used encapsulation in *h*-BN to avoid surface decomposition by oxygen and moisture from the air. Striving to utilize only scalable methods in our work, we took a different approach: immediately following removal from the process tube, we cap the substrate containing the 1D vdW $TaSe_3$ nanowires with spin-coated polymethyl methacrylate (C5 PMMA) resist under a nitrogen-atmosphere.

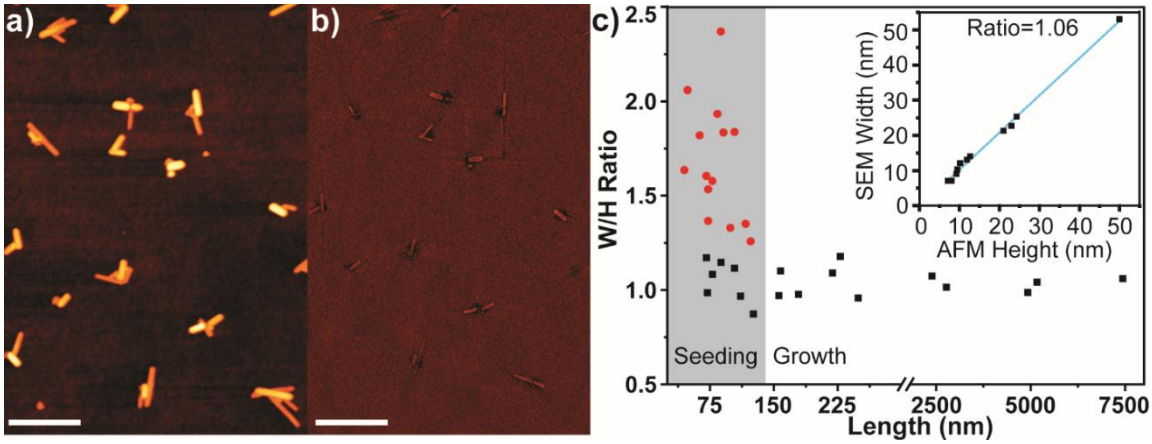


**Figure 4.8** a,b) Atomic force microscopy (AFM) and scanning electron microscopy (SEM) images, respectively, of the same population of $TaSe_3$ 1D vdW nanowire bundles (scalebar is 500 nm); c) The width to height ratio of the 1D vdW $TaSe_3$ nanowires at seeding (grey area) and as uniaxial growth continues: longer wires have a width-to-height aspect ratio of practical unity. The inset plots SEM width vs. the AFM height of the wires indicated by black markers in the main panel.

Subsequently, we characterize the nanowires by Raman spectroscopy through the PMMA film and then use the same resist film to fabricate electrical contacts. Care is taken to minimize the time between development and metal deposition so as to reduce air exposure of the sample. Immediately following metal liftoff, we again spin coat the sample with a layer of PMMA in a nitrogen glovebox. Subsequently, a second EBL process is performed to remove resist from the surface of the probe pads only. Electrical characterization proceeds in a nitrogen atmosphere.

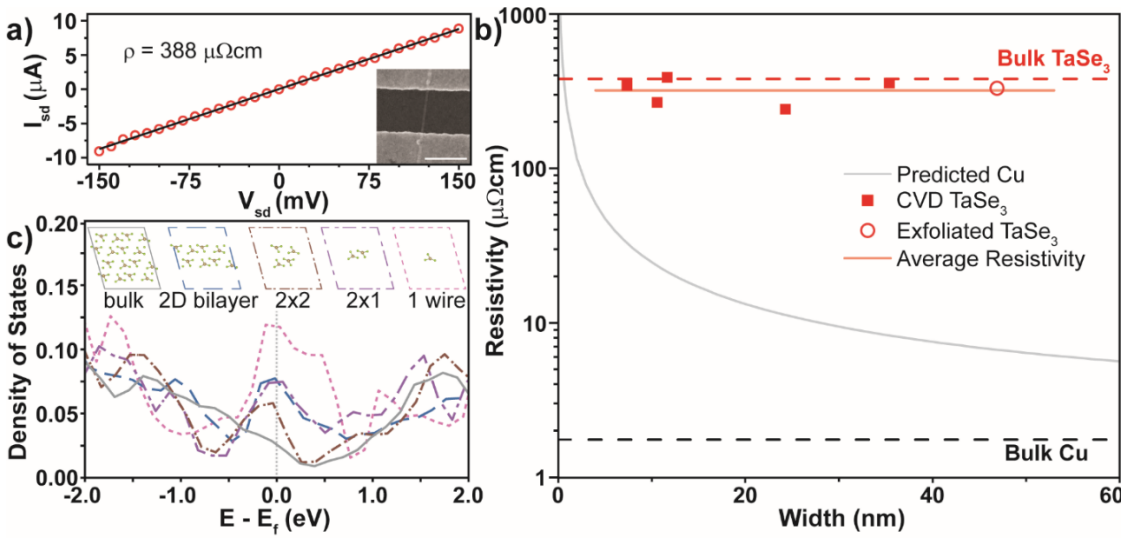


**Figure 4.9:** a) Source-Drain Current vs. Voltage ($I_{sd}$ vs. $V_{sd}$) for a 11.6 nm $TaSe_3$ nanowire; a linear dependence is observed in this two-probe measurement that corresponds to the current density shown on the y-axis and the resistivity highlighted. The inset shows an SEM image of a 1D vdW $TaSe_3$ nanowire bridging two electrodes (scalebar is 500 nm); b) resistivity of $TaSe_3$ nanowire bundles with width-to-height aspect ratios near unity (1.0-1.1) as a function of bundle width. For reference, we include bulk values for copper and $TaSe_3$ as dashed lines, as well as a prediction for the scaling of the copper resistivity with wire width based on Ref. [72] The smallest exfoliated nanowire of our prior studies is indicated as open dot. [66-68] c) Calculated density of states (DOS) near the Fermi level ($E_F$) for bulk $TaSe_3$, a 2D bilayer of wires, a 2×2 wire bundle, a 2×1 wire bundle and a single wire. The confined wire geometries have higher DOS at $E_F$ than the bulk material suggesting that quantum confinement does not adversely affect charge transport in $TaSe_3$.

Fig. 4.9a shows a typical current-voltage (I-V) diagram measured on a $TaSe_3$ nanowire with width and height of ~11.6 nm each. We use electrodes separated by 500 nm (inset). A linear I-V dependence is observed, from which a resistivity ρ of 388 μΩcm is obtained. The secondary y-axis of Fig. 4.9a shows the corresponding current density *J*.

We tested a large number of nanowires, each time followed by AFM and SEM characterization of their respective width and height. Fig. 4.9b shows the resistivity of wires with width ≤ 50 nm and cross section aspect ratios near unity (1.0-1.1). In a few cases we found wires that exhibited significant non-linear response for small voltage, which we ascribe to contact resistance. These were omitted from Fig. 4.9b. The figure reveals that the specific resistance of 1D vdW $TasSe_3$ nanowires is independent of the cross section of the wire bundle down to 7 nm in width and height. This presents a marked contrast to the behavior of copper at the nanoscale for which Fig. 4.9b includes a reference line based on the work of Steinhogel et al. [72] assuming surface *p* and grain boundary *R* scattering amplitudes of 0.5 and 0.6, respectively. At a few nanometer wire width, the resistivity of $TaSe_3$ becomes competitive to that of copper, assuming that a pinhole-free deposition of copper wires is possible at that width scale, which is not immediately apparent.[95]

If scattering does not limit the scaling of the conductivity of $TaSe_3$ nanowires, we explore whether quantum confinement perpendicular to the nanowire direction may do so. To this end, we assume that the conductivity of a metallic material in first order scales with its density of state (DOS) near the Fermi level ($E_F$) and calculate the DOS of various nanowire bundle configurations. We employ density functional theory as implemented in the Vienna Ab initio Simulation Package (VASP)[96] using the projector augmented wave method[86, 87]

and treating the electron exchange-correlation interaction by the generalized gradient approximation (GGA) functional of Perdew, Burke, and Ernzerhof (PBE).[88] All calculations use periodic boundary conditions and the Brillouin zone was sampled by a 2×7×2 Monkhorst−Pack k-point grid.[89]

Fig. 4.9c compares the density of states (DOS) of an infinite bulk of $TaSe_3$ (solid line) to an infinite 2D bilayer of wires, bundles of 2×2 and 2×1 wires, as well as a single wire. In each case we find considerable DOS near the Fermi level ($E_F$) and no band gap. Indeed, as the wire bundle is thinned to a bilayer and a finite number of wire stacks, the DOS near $E_F$ increases. This finding suggests that – at least for some wire bundle geometries – a higher native conductivity is possible than for the bulk case. We recognize, however, that this analysis omits fundamental stability limitations (such as the Mermin-Wagner-theorem[97]) yet we note that additional research is necessary to fathom their impact as shown for graphene.[98] The smallest wire bundle for which we obtained transport measurements had a width and height of ~ 7nm (Fig. 4.9b) and thus as few as ~10x10 wires in parallel; it is almost an order of magnitude larger than the computationally readily tractable ones of Fig. 4.9c.

Finally, we turn to the stability of the 1D vdW nanowires with regards to degradation under transport. Measurements of the low-frequency noise are commonly used to assess the quality and reliability of conventional[99-103] and novel 2D materials [67, 69, 104] for device applications. Changes in the noise spectra can serve as a convenient indicator of the onset of electromigration and other material degradation mechanisms. In the context of interconnect research, the low-frequency noise can provide a fast estimate of the device's

mean time to failure. The low-frequency noise measurements were performed using an experimental setup consisting of a "quiet" battery, a potentiometer biasing circuit, a low noise amplifier, and a spectrum analyzer; additional details have been reported elsewhere.[105, 106]

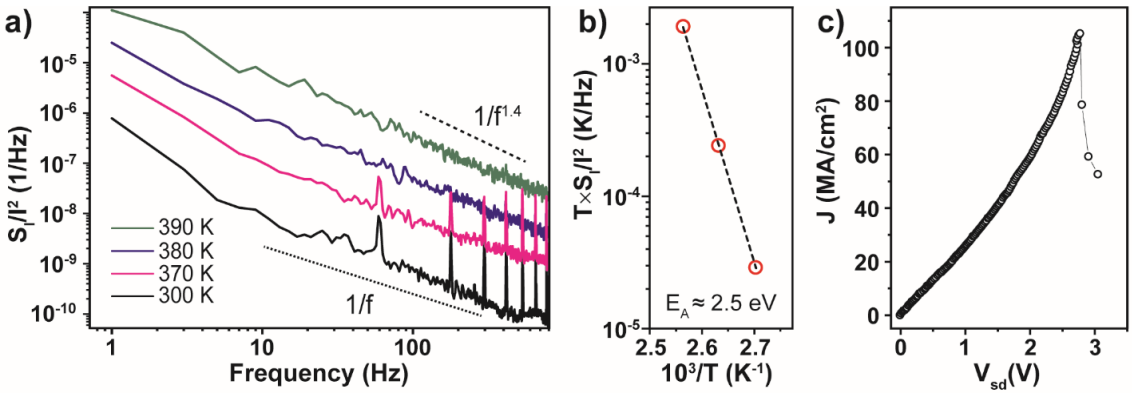


**Figure 4.10:** a) Normalized current noise spectral density of a ~10×10 nm$^2$ (width × height) CVD 1D vdW $TaSe_3$ nanowire bundle at different temperatures T using a source-drain voltage $V_{sd}$ of 0.1 V. b) Arrhenius plot of $T \times S_I/I^2$ vs. 1000/T for a frequency f of 11 Hz. The extracted activation energy $E_A$ is 2.57 eV. c) Current density J response of a ~7×7 nm$^2$ nanowire as the voltage is slowly increased. Failure occurs at a current density in excess of $10^8$ A/cm$^2$.

Figure 4.10a shows the normalized current noise spectral density $S_I/I^2$ as a function of frequency $f$ for a $TaSe_3$ nanowire with a cross-section of ~ 10×10 nm$^2$. The noise level $S_I/I^2$ of ~$10^{-8}$ Hz$^{-1}$ at $f$=10 Hz and $T$=300K in the downscaled CVD $TaSe_3$ nanowires is appreciably low. Although it is higher than measured in conventional metals[107, 108] and also for larger cross section exfoliated $TaSe_3$ nanowires,[67, 108] the latter is expected because the noise originating from a volume of independent fluctuators scales inversely proportional

to the size of the volume.[99] Indeed, one can write for the noise spectral density[99-101] $S_I/I^2=\alpha_H/Nf$, where $\alpha_H$ is the coefficient of proportionality referred to as the Hooge parameter, and $N=n\times V$, where n is the concentration of the charge carriers and $V$ is the volume of the sample. The noise levels of $10^{-9}$ $Hz^{-1}$ – $10^{-5}$ $Hz^{-1}$ are found in conventional transistors and other electronic devices.[101]

Fig. 4.10a reveals increase in the noise level with increasing temperature. The informative frequency range from 10 Hz to ~400 Hz exhibits a deviation from pure 1/*f* noise; approximately $1/f^{1.4}$ provides the best fit at elevated temperatures. This trend is consistent with observations on thicker exfoliated $TaSe_3$ nanowires.[67] In metals the deviation from 1/*f*-type behavior is commonly attributed to the onset of electromigration. We construct an Arrhenius plot of $T\times S_I/I^2$ vs. 1000/T (Fig. 4.10b) to extract the activation energy ($E_A$) for the noise inducing process in CVD 1D vdW $TaSe_3$ nanowires. The resultant value of ~2.5 eV is larger than that for exfoliated $TaSe_3$ nanowires[67] and more than twice that for electromigration in copper (0.76-1.10 eV) and aluminum (0.67- 1.14 eV ) using similar measurements.[102, 103, 108, 109] This finding suggests very good resistance of CVD $TaSe_3$ 1D vdW nanowire to electromigration.

The electromigration resilience of the CVD 1D vdW $TaSe_3$ nanowires is confirmed by successively increasing the voltage applied to a 7×7 $nm^2$ wire bundle (about 100 parallel Ta-$Se_3$ stacks in total). Fig. 4.10c shows that the wire bundle was able to sustain in excess of $10^8$ $A/cm^2$ before electrical breakdown. This current density is an order of magnitude higher than that found for thicker, exfoliated $TaSe_3$, and also slightly better than our previous findings for $ZrTe_3$.[69] We note that acquiring the dataset of Fig. 4.10c took almost

an hour of slowly increasing the bias, so that self-heating may have contributed to reduced overall current carrying capacity and increased susceptibility to electromigration. Embedding the nanowire with a better thermal sink than the underlying $SiO_2$ substrate and the surrounding PMMA resist may result in even higher sustained current densities.

**Summary**

The developed CVD growth process outlined shows that by altering process gases and cooling rates one can selectivity synthesis various phases of $MoTe_2$, from the semiconducting 2H phase to the novel 1T semi-metallic phase with relative ease. It also gave insight into the ability of a 1T/2H hybrid/mixed phase material to create a low resistance gate-able semiconducting 2D films. This characterization could allow the for future phase change configurations by tuning the phase alloying in a material.

We show that chemical vapor deposition allows the growth of $TaSe_3$ nanowires on a $SiO_2$ substrate that are competitive in resistivity to conventional metals scaled to sub-10-nanometer wire diameters, while offering significantly enhanced electromigration resilience and breakdown current. The growth proceeds at back-end-of-line compatible temperatures (~ 400°C) and because it takes just a few minutes, it has a comparatively low thermal budget impact. Future work will adapt prior findings on the spatially-selective growth of TMD materials[110-113] so as to generate the $TaSe_3$ nanowires not randomly dispersed on the sample but at desired locations only.

**Acknowledgements**

I would like to thank my mother and father, Cindy and Eugene, for their continued support throughout my life and instilling in me the work ethic and personal values needed to complete such an honor as receiving my PhD. I would also like to thank my family, friends, lab mates, and roommates for their continued support, understanding, and friendship on this journey.

Additionally, I would like to thank my Professor, Dr. Ludwig Bartels for his support and guidance throughout my graduate career and the extraordinary opportunity to receive my PhD.

I would also like to recognize:

The National Science Foundation, C-SPIN, MARCO, DARPA, US Air Force Office of Scientific Research, Semiconductor Research Corporation, the SRC STARnet program, and Intel for their support in funding these projects.

**References:**


1. Sebenik, R. F.; Burkin, A. R.; Dorfler, R. R.; Laferty, J. M.; Leichtfried, G.; Meyer-Grünow, H.; Mitchell, P. C. H.; Vukasovich, M. S.; Church, D. A.; Riper, G. G. V.; Gilliland, J. C.; Thielke, S. A., Molybdenum and Molybdenum Compounds. Ullmann's Encyclopedia of Industrial Chemistry, 2012; Vol. 23, pp 521-566.

2. Karmadon.Af, Molybdenum-Disulphide Lubrication In Pressure Working Of Metals. *Russian Engineering Journal-Ussr* **1969,** *49* (9), 78-&.

3. Knappwos.A; Thieme, F., Kinetic Of Reaction Effects In Solid Lubrication Of Iron With Molybdenum Disulphide. *Zeitschrift Fur Physikalische Chemie-Frankfurt* **1969,** *63* (1-4), 1.

4. Farr, J. P. G., Molybdenum-Disulphide In Lubrication - Review. *Wear* **1975,** *35* (1), 1-22.

5. Winer, W. O., Molybdenum Disulphide As A Lubricant - A Review Of Fundamental Knowledge. *Wear* **1967,** *10* (6), 422.

6. Bell, M. E.; Findley, J. H., Molybdenite as a new lubricant. Physical Review, 1941; Vol. 59, p 922.

7. Feynman, R. In *There's Plenty of Room at the Bottom*, American Physical Society, Pasadena, California, Caltech Engineering and Science: Pasadena, California, 1959; pp 22-36.

8. Lv, R.; Robinson, J. A.; Schaak, R. E.; Sun, D.; Sun, Y. F.; Mallouk, T. E.; Terrones, M., Transition Metal Dichalcogenides and Beyond: Synthesis, Properties, and Applications of Single- and Few-Layer Nanosheets. *Accounts of Chemical Research* **2015,** *48* (1), 56-64.

9. Frindt, R. F.; Yoffe, A. D., Physical Properties Of Layer Structures - Optical Properties And Photoconductivity Of Thin Crystals Of Molybdenum Disulphide. *Proceedings of the Royal Society of London Series a-Mathematical and Physical Sciences* **1963,** *273* (1352), 69.

10. Murphy, D. W.; Hull, G. W., Monodispersed Tantalum Disulfide And Adsorption Complexes With Cations. *Journal of Chemical Physics* **1975,** *62* (3), 973-978.

11. Liu, C.; Singh, O.; Joensen, P.; Curzon, A. E.; Frindt, R. F., X-RAY And Electron-Microscopy Studies Of Single-Layer $TaS_2$ And $NbS_2$. *Thin Solid Films* **1984,** *113* (2), 165-172.

12. Joensen, P.; Frindt, R. F.; Morrison, S. R., Single-Layer $MoS_2$. *Materials Research Bulletin* **1986,** *21* (4), 457-461.

13. Furimsky, E., Role Of $MoS_2$ And $WS_2$ In Hydrodesulfurization. *Catalysis Reviews-Science and Engineering* **1980,** *22* (3), 371-400.

14. Chianelli, R. R.; Prestridge, E. B.; Pecoraro, T. A.; Deneufville, J. P., Molybdenum-Disulfide In The Poorly Crystalline RAG Structure. *Science* **1979,** *203* (4385), 1105-1107.

15. Debeer, V. H. J.; Dahlmans, J. G. J.; Smeets, J. G. M., Hydrodesulfurization And Hydrogenation Properties Of Promoted $MoS_2$ And $WS_2$ Catalysts Under Medium Pressure Conditions. *Journal of Catalysis* **1976,** *42* (3), 467-470.

16. Furimsky, E.; Amberg, C. H., Role Of Cobalt In Unsupported $MoS_2$ Hydrodesulfurization Catalysts. *Canadian Journal of Chemistry-Revue Canadienne De Chimie* **1975,** *53* (17), 2542-2547.

17. Canesson, P.; Grange, P., Photoelectron-Spectroscopy Of $MoS_2$-$Co_9S_8$ System Study Of Hydrodesulfurization Catalysts With A Low Cobalt Content. *Comptes Rendus Hebdomadaires Des Seances De L Academie Des Sciences Serie C* **1975,** *281* (19), 757-759.

18. Novoselov, K. S.; Geim, A. K.; Morozov, S. V.; Jiang, D.; Zhang, Y.; Dubonos, S. V.; Grigorieva, I. V.; Firsov, A. A., Electric field effect in atomically thin carbon films. *Science* **2004,** *306* (5696), 666-669.

19. Splendiani, A.; Sun, L.; Zhang, Y. B.; Li, T. S.; Kim, J.; Chim, C. Y.; Galli, G.; Wang, F., Emerging Photoluminescence in Monolayer $MoS_2$. *Nano Letters* **2010,** *10* (4), 1271-1275.

20. Mak, K. F.; Lee, C.; Hone, J.; Shan, J.; Heinz, T. F., Atomically Thin MoS2: A New Direct-Gap Semiconductor. *Physical Review Letters* **2010,** *105* (13).

21. Splendiani, A.; Sun, L.; Zhang, Y. B.; Li, T. S.; Kim, J.; Chim, C. Y.; Galli, G.; Wang, F., Emerging photoluminescence in monolayer $MoS_2$ *Nano Lett.* **2010,** *10* (4), 1271-1275.

22. Eda, G.; Yamaguchi, H.; Voiry, D.; Fujita, T.; Chen, M. W.; Chhowalla, M., Photoluminescence from Chemically Exfoliated $MoS_2$. *Nano Letters* **2011,** *11* (12), 5111-5116.

23. Mak, K. F.; He, K. L.; Shan, J.; Heinz, T. F., Control of valley polarization in monolayer $MoS_2$ by optical helicity. *Nat Nanotechnol* **2012,** *7* (8), 494-498.

24. Cao, T.; Wang, G.; Han, W. P.; Ye, H. Q.; Zhu, C. R.; Shi, J. R.; Niu, Q.; Tan, P. H.; Wang, E.; Liu, B. L.; Feng, J., Valley-selective circular dichroism of monolayer molybdenum disulphide. *Nat. Comm.* **2012,** *3*, 887.

25. Xiao, D.; Liu, G.-B.; Feng, W.; Xu, X.; Yao, W., Coupled Spin and Valley Physics in Monolayers of $MoS_2$ and Other Group-VI Dichalcogenides. *Phys. Rev. Lett.* **2012,** *108* (19), 196802.

26. Neal, A. T.; Liu, H.; Gu, J. J.; Ye, P. D. D., Magneto-transport in $MoS_2$: Phase Coherence, Spin-Orbit Scattering, and the Hall Factor. *ACS Nano* **2013,** *7* (8), 7077-7082.

27. Ruppert, C.; Aslan, O. B.; Heinz, T. F., Optical Properties and Band Gap of Single- and Few-Layer $MoTe_2$ Crystals. *Nano Letters* **2014,** *14* (11), 6231-6236.

28. Chen, B.; Sahin, H.; Suslu, A.; Ding, L.; Bertoni, M. I.; Peeters, F. M.; Tongay, S., Environmental Changes in MoTe2 Excitonic Dynamics by Defects-Activated Molecular Interaction. *Acs Nano* **2015,** *9* (5), 5326-5332.

29. Liu, H. S.; Han, N. N.; Zhao, J. J., Atomistic insight into the oxidation of monolayer transition metal dichalcogenides: from structures to electronic properties. *Rsc Advances* **2015,** *5* (23), 17572-17581.

30. Kappera, R.; Voiry, D.; Yalcin, S. E.; Branch, B.; Gupta, G.; Mohite, A. D.; Chhowalla, M., Phase-engineered low-resistance contacts for ultrathin $MoS_2$ transistors. *Nat. Mater.* **2014,** *13*, 1128–1134.

31. Duerloo, K. A. N.; Li, Y.; Reed, E. J., Structural phase transitions in two-dimensional Mo- and W-dichalcogenide monolayers. *Nat. Comm.* **2014,** *5*, 4214.

32. Dawson, W. G.; Bullett, D. W., Electronic-Structure and Crystallography of $MoTe_2$ and $WTe_d$. *Journal of Physics C-Solid State Physics* **1987,** *20* (36), 6159-6174.

33. Kan, M.; Nam, H. G.; Lee, Y. H.; Sun, Q., Phase stability and Raman vibration of the molybdenum ditelluride ($MoTe_2$) monolayer. *Physical Chemistry Chemical Physics* **2015,** *17* (22), 14866-14871.

34. Li, Y.; Duerloo, K. A. N.; Wauson, K.; Reed, E. J., Structural semiconductor-to-semimetal phase transition in two-dimensional materials induced by electrostatic gating. *Nature Communications* **2016,** *7*.

35. Park, J. C.; Yun, S. J.; Kim, H.; Park, J. H.; Chae, S. H.; An, S. J.; Kim, J. G.; Kim, S. M.; Kim, K. K.; Lee, Y. H., Phase-Engineered Synthesis of Centimeter-Scale 1T '- and 2H-Molybdenum Ditelluride Thin Films. *Acs Nano* **2015,** *9* (6), 6548-6554.

36. Cho, S.; Kim, S.; Kim, J. H.; Zhao, J.; Seok, J.; Keum, D. H.; Baik, J.; Choe, D. H.; Chang, K. J.; Suenaga, K.; Kim, S. W.; Lee, Y. H.; Yang, H., Phase patterning for ohmic homojunction contact in $MoTe_2$. *Science* **2015,** *349* (6248), 625-628.

37. Song, S.; Keum, D. H.; Cho, S.; Perello, D.; Kim, Y.; Lee, Y. H., Room Temperature Semiconductor-Metal Transition of $MoTe_2$ Thin Films Engineered by Strain. *Nano Letters* **2016,** *16* (1), 188-193.

38. Pradhan, N. R.; Rhodes, D.; Feng, S. M.; Xin, Y.; Memaran, S.; Moon, B. H.; Terrones, H.; Terrones, M.; Balicas, L., Field-Effect Transistors Based on Few-Layered α-$MoTe_2$. *Acs Nano* **2014,** *8* (6), 5911-5920.

39. Nakaharai, S.; Yamamoto, M.; Ueno, K.; Tsukagoshi, K., Carrier Polarity Control in α-$MoTe_2$ Schottky Junctions Based on Weak Fermi-Level Pinning. *ACS Applied Materials & Interfaces* **2016,** *8* (23), 14732-14739.

40. Lin, Y.-F.; Xu, Y.; Wang, S.-T.; Li, S.-L.; Yamamoto, M.; Aparecido-Ferreira, A.; Li, W.; Sun, H.; Nakaharai, S.; Jian, W.-B.; Ueno, K.; Tsukagoshi, K., Ambipolar $MoTe_2$ Transistors and Their Applications in Logic Circuits. *Advanced Materials* **2014,** *26* (20), 3263-3269.

41. Pezeshki, A.; Hosseini Shokouh, S. H.; Jeon, P. J.; Shackery, I.; Kim, J. S.; Oh, I.-K.; Jun, S. C.; Kim, H.; Im, S., Static and Dynamic Performance of Complementary Inverters Based on Nanosheet α-$MoTe_2$ p-Channel and $MoS_2$ n-Channel Transistors. *ACS Nano* **2016,** *10* (1), 1118-1125.

42. Nakaharai, S.; Yamamoto, M.; Ueno, K.; Lin, Y.-F.; Li, S.-L.; Tsukagoshi, K., Electrostatically Reversible Polarity of Ambipolar α-$MoTe_2$ Transistors. *ACS Nano* **2015,** *9* (6), 5976-5983.

43. Yamamoto, M.; Wang, S. T.; Ni, M. Y.; Lin, Y. F.; Li, S. L.; Aikawa, S.; Jian, W. B.; Ueno, K.; Wakabayashi, K.; Tsukagoshi, K., Strong Enhancement of Raman Scattering from a Bulk-Inactive Vibrational Mode in Few-Layer $MoTe_2$. *Acs Nano* **2014,** *8* (4), 3895-3903.

44. Roy, A.; Movva, H. C. P.; Satpati, B.; Kim, K.; Dey, R.; Rai, A.; Pramanik, T.; Guchhait, S.; Tutuc, E.; Banerjee, S. K., Structural and Electrical Properties of $MoTe_2$ and $MoSe_2$ Grown by Molecular Beam Epitaxy. *ACS Applied Materials & Interfaces* **2016,** *8* (11), 7396-7402.

45. Zhou, L.; Xu, K.; Zubair, A.; Liao, A. D.; Fang, W. J.; Ouyang, F. P.; Lee, Y. H.; Ueno, K.; Saito, R.; Palacios, T.; Kong, J.; Dresselhaus, M. S., Large-Area Synthesis of High-Quality Uniform Few-Layer $MoTe_2$. *J. Am. Chem. Soc.* **2015,** *137* (37), 11892-11895.

46. Naylor, C. H.; Parkin, W. M.; Ping, J. L.; Gao, Z. L.; Zhou, Y. R.; Kim, Y.; Streller, F.; Carpick, R. W.; Rappe, A. M.; Drndic, M.; Kikkawa, J. M.; Johnson, A. T. C., Monolayer Single-Crystal 1T '-$MoTe_2$ Grown by Chemical Vapor Deposition Exhibits Weak Antilocalization Effect. *Nano Lett.* **2016,** *16* (7), 4297-4304.

47. Zhou, Y.; Reed, E. J., Structural Phase Stability Control of Monolayer $MoTe_2$ with Adsorbed Atoms and Molecules. *J. Phys. Chem. C* **2015,** *119* (37), 21674-21680.

48. Biltz, W.; Kocher, A., Articles on the systematic related system 82 - The tantalum/sulphur system. *Zeitschrift Fur Anorganische Und Allgemeine Chemie* **1938,** *238* (1), 81-93.

49. Ariya, S. M.; Zaslavskii, A. I.; Matveeva, I. I., Khimiya Soedinenii Peremennogo Sostava .4. Sistema Tantal-Selen. *Zhurnal Obshchei Khimii* **1956,** *26* (9), 2373-2375.

50. Bjerkelund, E.; Kjekshus, A., On the Properties of $TaS_3$, $TaSe_3$ and $TaTe_4$. *Zeitschrift Fur Anorganische Und Allgemeine Chemie* **1964,** *328* (5-6), 235-242.

51. Bjerkelund, E.; Fermor, J. H.; Kjekshus, A., On Properties Of $TaS_3$ AND $TaSe_3$. *Acta Chemica Scandinavica* **1966,** *20* (7), 1836.

52. Monceau, P.; Peyrard, J.; Richard, J.; Molinie, P., Superconductivity Of Linear Trichalcogenide $NbSe_3$ Under Pressure. *Physical Review Letters* **1977,** *39* (3), 161-164.

53. Vantendeloo, G.; Vanlanduyt, J.; Amelinckx, S., Electron-Diffraction Evidence For a One-Dimensional Peierls Distortion in a Transiton Metal Trichalcogenide $TaS_3$. *Physica Status Solidi a-Applied Research* **1977,** *43* (2), K137-&.

54. Chhowalla, M.; Shin, H. S.; Eda, G.; Li, L. J.; Loh, K. P.; Zhang, H., The chemistry of two-dimensional layered transition metal dichalcogenide nanosheets. *Nat Chem* **2013,** *5* (4), 263-75.

55. Bernardi, M.; Palummo, M.; Grossman, J. C., Extraordinary Sunlight Absorption and One Nanometer Thick Photovoltaics Using Two-Dimensional Monolayer Materials. *Nano Letters* **2013,** *13* (8), 3664-3670.

56. Bhimanapati, G. R.; Lin, Z.; Meunier, V.; Jung, Y.; Cha, J.; Das, S.; Xiao, D.; Son, Y.; Strano, M. S.; Cooper, V. R.; Liang, L. B.; Louie, S. G.; Ringe, E.; Zhou, W.; Kim, S. S.; Naik, R. R.; Sumpter, B. G.; Terrones, H.; Xia, F. N.; Wang, Y. L.; Zhu, J.; Akinwande, D.; Alem, N.; Schuller, J. A.; Schaak, R. E.; Terrones, M.; Robinson, J. A., Recent Advances in Two-Dimensional Materials beyond Graphene. *ACS Nano* **2015,** *9* (12), 11509-11539.

57. Empante, T. A.; Zhou, Y.; Klee, V.; Nguyen, A. E.; Lu, I. H.; Valentin, M. D.; Naghibi Alvillar, S. A.; Preciado, E.; Berges, A. J.; Merida, C. S.; Gomez, M.; Bobek, S.; Isarraraz, M.; Reed, E. J.; Bartels, L., Chemical Vapor Deposition Growth of Few-Layer $MoTe_2$ in the 2H, 1T′, and 1T Phases: Tunable Properties of $MoTe_2$ Films. *ACS Nano* **2017,** *11*, 900.

58. Mak, K. F.; Lee, C.; Hone, J.; Shan, J.; Heinz, T. F., Atomically thin $MoS_2$: a new direct-gap semiconductor. *Phys. Rev. Lett.* **2010,** *105* (13), 136805.

59. Castro Neto, A. H.; Guinea, F.; Peres, N. M. R.; Novoselov, K. S.; Geim, A. K., The electronic properties of graphene. *Rev. Mod. Phys.* **2009,** *81* (1), 109.

60. Lee, C.; Wei, X. D.; Kysar, J. W.; Hone, J., Measurement of the elastic properties and intrinsic strength of monolayer graphene. *Science* **2008,** *321* (5887), 385-388.

61. Zhang, Y. B.; Tan, Y. W.; Stormer, H. L.; Kim, P., Experimental observation of the quantum Hall effect and Berry's phase in graphene. *Nature* **2005,** *438* (7065), 201-204.

62. Lukatskaya, M. R.; Mashtalir, O.; Ren, C. E.; Dall'Agnese, Y.; Rozier, P.; Taberna, P. L.; Naguib, M.; Simon, P.; Barsoum, M. W.; Gogotsi, Y., Cation Intercalation and High Volumetric Capacitance of Two-Dimensional Titanium Carbide. *Science* **2013,** *341* (6153), 1502-1505.

63. Naguib, M.; Mashtalir, O.; Carle, J.; Presser, V.; Lu, J.; Hultman, L.; Gogotsi, Y.; Barsoum, M. W., Two-Dimensional Transition Metal Carbides. *Acs Nano* **2012,** *6* (2), 1322-1331.

64. Naguib, M.; Mochalin, V. N.; Barsoum, M. W.; Gogotsi, Y., 25th Anniversary Article: MXenes: A New Family of Two-Dimensional Materials. *Advanced Materials* **2014,** *26* (7), 992-1005.

65. Khazaei, M.; Arai, M.; Sasaki, T.; Chung, C. Y.; Venkataramanan, N. S.; Estili, M.; Sakka, Y.; Kawazoe, Y., Novel Electronic and Magnetic Properties of Two-Dimensional Transition Metal Carbides and Nitrides. *Adv. Funct. Mater.* **2013,** *23* (17), 2185-2192.

66. Geremew, A.; Rumyantsev, S.; Bloodgood, M. A.; Salguero, T. T.; Balandin, A. A., Unique features of the generation–recombination noise in quasi-one-dimensional van der Waals nanoribbons. *Nanoscale* **2018,** *10.1039/C8NR06984K*.

67. Liu, G. X.; Rumyantsev, S.; Bloodgood, M. A.; Salguero, T. T.; Shur, M.; Balandin, A. A., Low-Frequency Electronic Noise in Quasi-1D $TaSe_3$ van der Waals Nanowires. *Nano Letters* **2017,** *17* (1), 377-383.

68. Stolyarov, M. A.; Liu, G. X.; Bloodgood, M. A.; Aytan, E.; Jiang, C. L.; Samnakay, R.; Salguero, T. T.; Nika, D. L.; Rumyantsev, S. L.; Shur, M. S.; Bozhilov, K. N.; Balandin, A. A., Breakdown current density in h-BN-capped quasi-1D $TaSe_3$ metallic nanowires: prospects of interconnect applications. *Nanoscale* **2016,** *8* (34), 15774-15782.

69. Geremew, A.; Bloodgood, M. A.; Aytan, E.; Woo, B. W. K.; Corber, S. R.; Liu, G.; Bozhilov, K.; Salguero, T. T.; Rumyantsev, S.; Rao, M. P.; Balandin, A. A., Current Carrying Capacity of Quasi-1D $ZrTe_3$ Van Der Waals Nanoribbons. *IEEE Electr. Dev. L.* **2018,** *39* (5), 735-738.

70. Gall, D., Electron mean free path in elemental metals. *J. Appl. Phys.* **2016,** *119* (8), 085101.

71. Steinhogl, W.; Schindler, G.; Steinlesberger, G.; Traving, M.; Engelhardt, M., Comprehensive study of the resistivity of copper wires with lateral dimensions of 100 nm and smaller. *J. Appl. Phys.* **2005,** *97* (2), 023706

72. Steinhogl, W.; Schindler, G.; Steinlesberger, G.; Engelhardt, M., Size-dependent resistivity of metallic wires in the mesoscopic range. *Phys. Rev. B* **2002,** *66* (7).

73. Li, B. Z.; Sullivan, T. D.; Lee, T. C.; Badami, D., Reliability challenges for copper interconnects. *Microelectronics Reliability* **2004,** *44* (3), 365-380.

74. Lloyd, J. R.; Clement, J. J., Electromigration damage due to copper depletion in Al/Cu alloy conductors. *Applied Physics Letters* **1996,** *69* (17), 2486-2488.

75. Hu, C. K.; Luther, B.; Kaufman, F. B.; Hummel, J.; Uzoh, C.; Pearson, D. J., Copper Interconnection Integration and Reliability. *Thin Solid Films* **1995,** *262* (1-2), 84-92.

76. Kapur, P.; Chandra, G.; McVittie, J. P.; Saraswat, K. C., Technology and reliability constrained future copper interconnects - Part II: Performance implications. *IEEE Trans. Electron Devices* **2002,** *49* (4), 598-604.

77. Heath, J.; Taylor, N., *Raman Microscopy*. John Wiley & Sons, Inc.: 2017.

78. SPM modi and measurement methods. https://www.dme-spm.com/spmmodi.html.

79. Mann, J.; Sun, D.; Ma, Q.; Chen, J.-R.; Preciado, E.; Ohta, T.; Diaconescu, B.; Yamaguchi, K.; Tran, T.; Wurch, M.; Magnone, K.; Heinz, F. T.; Kellogg, L. G.; Kawakami, R.; Bartels, L., Facile growth of monolayer $MoS_2$ film areas on $SiO_2$. *The European Physical Journal B* **2013,** *86* (5), 1-4.

80. Mann, J.; Sun, D.; Ma, Q.; Chen, J.-R.; Preciado, E.; Ohta, T.; Diaconescu, B.; Yamaguchi, K.; Tran, T.; Wurch, M.; Magnone, K.; Heinz, T. F.; Kellogg, G. L.; Kawakami, R.; Bartels, L., Facile growth of monolayer $MoS_2$ film areas on $SiO_2$. *The European Physical Journal B* **2013,** *86* (5), 1-4.

81. Mann, J.; Ma, Q.; Odenthal, P. M.; Isarraraz, M.; Le, D.; Preciado, E.; Barroso, D.; Yamaguchi, K.; Palacio, G. V.; Nguyen, A.; Tran, T.; Wurch, M.; Nguyen, A.; Klee, V.; Bobek, S.; Sun, D. Z.; Heinz, T. F.; Rahman, T. S.; Kawakami, R.; Bartels, L., 2-Dimensional Transition Metal Dichalcogenides with Tunable Direct Band Gaps: $MoS_{2(1-x)}Se_{2x}$ Monolayers. *Adv. Mater.* **2014,** *26* (9), 1399-1404.

82. Empante, T. A.; Zhou, Y.; Klee, V.; Nguyen, A. E.; Lu, I. H.; Valentin, M. D.; Alvillar, S. A. N.; Preciado, E.; Berges, A. J.; Merida, C. S.; Gomez, M.; Bobek, S.; Isarraraz, M.; Reed, E. J.; Bartels, L., Chemical Vapor Deposition Growth of Few Layer $MoTe_2$ in the 2H, 1T ', and 1T Phases: Tunable Properties of $MoTe_2$ Films. *Acs Nano* **2017,** *11* (1), 900-905.

83. Tsen, A. W.; Hovden, R.; Wang, D.; Kim, Y. D.; Okamoto, J.; Spoth, K. A.; Liu, Y.; Lu, W. J.; Sun, Y. P.; Hone, J. C.; Kourkoutis, L. F.; Kim, P.; Pasupathy, A. N., Structure and control of charge density waves in two-dimensional 1T-$TaS_2$. *Proc. Natl. Acad. Sci. USA* **2015,** *112* (49), 15054-15059.

84. Keum, D. H.; Cho, S.; Kim, J. H.; Choe, D. H.; Sung, H. J.; Kan, M.; Kang, H.; Hwang, J. Y.; Kim, S. W.; Yang, H.; Chang, K. J.; Lee, Y. H., Bandgap opening in few-layered monoclinic $MoTe_2$. *Nature Physics* **2015,** *11* (6), 482-U144.

85. Kresse, G.; Furthmuller, J., Efficient iterative schemes for ab initio total-energy calculations using a plane-wave basis set. *Phys. Rev. B* **1996,** *54* (16), 11169-11186.

86. Blochl, P. E., Projector Augmented-Wave Method. *Phys. Rev. B* **1994,** *50* (24), 17953-17979.

87. Kresse, G.; Joubert, D., From ultrasoft pseudopotentials to the projector augmented-wave method. *Phys. Rev. B* **1999,** *59* (3), 1758-1775.

88. Perdew, J. P.; Burke, K.; Ernzerhof, M., Generalized gradient approximation made simple. *Phys. Rev. Lett.* **1996,** *77* (18), 3865-3868.

89. Monkhorst, H. J.; Pack, J. D., Special Points for Brillouin-Zone Integrations. *Phys. Rev. B* **1976,** *13* (12), 5188-5192.

90. Empante, T. A.; Martinez, A.; Wurch, M.; Zhu, Y. B.; Geremew, A. K.; Yamaguchi, K.; Isarraraz, M.; Rumyantsev, S.; Reed, E. J.; Balandin, A. A.; Bartels, L.,

Low Resistivity and High Breakdown Current Density of 10 nm Diameter van der Waals $TaSe_3$ Nanowires by Chemical Vapor Deposition. *Nano Letters* **2019,** *19* (7), 4355-4361.

91. Canadell, E.; Rachidi, I. E. I.; Pouget, J. P.; Gressier, P.; Meerschaut, A.; Rouxel, J.; Jung, D.; Evain, M.; Whangbo, M. H., Comparison of the Electronic-Structures of Layered Transition-Metal Trichalcogenides $TaSe_3$, $TaS_3$, and $NbSe_3$. *Inorganic Chemistry* **1990,** *29* (7), 1401-1407.

92. Heidenreich, J.; Edelstein, D.; Goldblatt, R.; Cote, W.; Uzoh, C.; Lustig, N.; McDevitt, T.; Stamper, A.; Simon, A.; Dukovic, J.; Andricacos, P.; Wachnik, R.; Rathore, H.; Katsetos, T.; McLaughlin, P.; Luce, S.; Slattery, J.; Ieee, E. D. S., Copper dual damascene wiring for sub-0.25 μm CMOS technology. *Proceedings of the Ieee 1998 International Interconnect Technology Conference* **1998**, 151-153.

93. Bohr, M.; Ahmed, S. S.; Ahmed, S. U.; Bost, M.; Ghani, T.; Greason, J.; Hainsey, R.; Jan, C.; Packan, P.; Sivakumar, S.; Thompson, S.; Tsai, J.; Yang, S.; Ieee, A high performance 0.25 μm logic technology optimized for 1.8V operation. *Iedm - International Electron Devices Meeting, Technical Digest 1996* **1996**, 847-850.

94. Fischer, K.; Agostinelli, M.; Allen, C.; Bahr, D.; Bost, M.; Charvat, P.; Chikarmane, V.; Fu, Q.; Ganpule, C.; Haran, M.; Heckscher, M.; Hiramatsu, H.; Hwang, E.; Jain, P.; Jin, I.; Kasim, R.; Kosaraju, S.; Lee, K. S.; Liu, H.; McFadden, R.; Nigam, S.; Patel, R.; Pelto, C.; Plekhanov, P.; Prince, M.; Puls, C.; Rajamani, S.; Rao, D.; Reese, P.; Rosenbaum, A.; Sivakumar, S.; Song, B.; Uncuer, M.; Williams, S.; Yang, M.; Yashar, P.; Natarajan, S., Low-k Interconnect Stack with multi-layer Air Gap and Tri-Metal-Insulator-Metal Capacitors for 14nm High Volume Manufacturing. *2015 IEEE International Interconnect Technology Conference and 2015 IEEE Materials for Advanced Metallization Conference (IITC/MAM)* **2015**, 5-7.

95. Wang, T. C.; Wang, Y. L.; Hsieh, T. E.; Chang, S. C.; Cheng, Y. L., Copper voids improvement for the copper dual damascene interconnection process. *Journal of Physics and Chemistry of Solids* **2008,** *69* (2-3), 566-571.

96. Kresse, G.; Furthmüller, J., Efficiency of ab-initio total energy calculations for metals and semiconductors using a plane-wave basis set. *Comput. Mat. Sci.* **1996,** *6*, 15.

97. Mermin, N. D.; Wagner, H., Absence of Ferromagnetism or Antiferromagnetism in One- or 2-Dimensional Isotropic Heisenberg Models. *Phys. Rev. Lett.* **1966,** *17* (22), 1133-&.

98. O'Hare, A.; Kusmartsev, F. V.; Kugel, K. I., A Stable "Flat" Form of Two-Dimensional Crystals: Could Graphene, Silicene, Germanene Be Minigap Semiconductors? *Nano Lett.* **2012,** *12* (2), 1045-1052.

99. Dutta, P.; Horn, P. M., Low-Frequency Fluctuations in Solids: 1/f Noise. *Rev. Mod. Phys.* **1981,** *53* (3), 497-516.

100. Vandamme, L. K. J., Noise as a Diagnostic-Tool for Quality and Reliability of Electronic Devices. *IEEE Trans. Electron Devices* **1994,** *41* (11), 2176-2187.

101. Balandin, A. A., *Noise and Fluctuations Control in Electronic Devices. Los Angeles, CA, USA: American Scientific Publishers, Aug. 2002*.

102. Beyne, S.; Croes, K.; De Wolf, I.; Tokei, Z., 1/f noise measurements for faster evaluation of electromigration in advanced microelectronics interconnections. *J. Appl. Phys.* **2016,** *119* (18), 184302.

103. Bagnoli, P. E.; Ciofi, C.; Neri, B.; Pennelli, G., Electromigration in Al based stripes: Low frequency noise measurements and MTF tests. *Microelectronics and Reliability* **1996,** *36* (7-8), 1045-1050.

104. Balandin, A. A., Low-frequency 1/f noise in graphene devices. *Nat. Nanotechnol.* **2013,** *8* (8), 549-555.

105. Rumyantsev, S.; Liu, G.; Stillman, W.; Shur, M.; Balandin, A. A., Electrical and noise characteristics of graphene field-effect transistors: ambient effects, noise sources and physical mechanisms. *J. Phys.-Condens. Mat.* **2010,** *22* (39), 395302.

106. Liu, G. X.; Rumyantsev, S.; Bloodgood, M. A.; Salguero, T. T.; Balandin, A. A., Low-Frequency Current Fluctuations and Sliding of the Charge Density Waves in Two-Dimensional Materials. *Nano Letters* **2018,** *18* (6), 3630-3636.

107. Dutta, P.; Dimon, P.; Horn, P. M., Energy Scales for Noise Processes in Metals. *Phys. Rev. Lett.* **1979,** *43* (9), 646-649.

108. Koch, R. H.; Lloyd, J. R.; Cronin, J., 1/F Noise and Grain-Boundary Diffusion in Aluminum and Aluminum-Alloys. *Phys. Rev. Lett.* **1985,** *55* (22), 2487-2490.

109. Chen, T. M.; Yassine, A. M., Electrical Noise and VLSI Interconnect Reliability. *IEEE Trans. Electron Devices* **1994,** *41* (11), 2165-2172.

110. Liao, I.; Barroso, D.; nguyen, A.; Duong, N.; Yurek, Q.; merida, C. S.; Pena, P.; Lu, I.-H.; valentin, M.; Stecklein, G.; Bartels, L., Hybrid Single-Layer/Bulk Tungsten Diselenide Transistors by Lithographic Encoding of Material Thickness in Chemical Vapor Deposition. *2D Mat.* **2018,** *6*, 015017.

111. Sun, D. Z.; Nguyen, A. E.; Barroso, D.; Zhang, X.; Preciado, E.; Bobek, S.; Klee, V.; Mann, J.; Bartels, L., Chemical vapor deposition growth of a periodic array of single-layer $MoS_2$ islands via lithographic patterning of an $SiO_2$/Si substrate. *2D Mat.* **2015,** *2* (4), 045014.

112. Gong, C. H.; Hu, K.; Wang, X. P.; Wangyang, P. H.; Yan, C. Y.; Chu, J. W.; Liao, M.; Dai, L. P.; Zhai, T. Y.; Wang, C.; Li, L.; Xiong, J., 2D Nanomaterial Arrays for Electronics and Optoelectronics. *Adv. Funct. Mater.* **2018,** *28* (16), 1706559.

113. Young, J. R.; Chilcote, M.; Barone, M.; Xu, J. S.; Katoch, J.; Luo, Y. K.; Mueller, S.; Asel, T. J.; Fullerton-Shirey, S. K.; Kawakami, R.; Gupta, J. A.; Brillson, L. J.; Johnston-Halperin, E., Uniform large-area growth of nanotemplated high-quality monolayer $MoS_2$. *Appl. Phys. Lett.* **2017,** *110* (26), 263103